



RESEARCH ARTICLE

10.1002/2015JD023386

Key Points:

- Ocean gains heat in calm weather and loses heat in disturbed weather
- Thick and less stratified remnant layer can suppress surface re-stratification
- Insufficient recovery of upper ocean heat content delays Taiwan Low development

Supporting Information:

- Figures S1–S6 and Table S1

Correspondence to:

P.-L. Lin,
tliam@pblap.atm.ncu.edu.tw

Citation:

Kueh, M.-T., and P.-L. Lin (2015), Upper ocean response and feedback to spring weather over the Kuroshio in the East China Sea: A coupled atmosphere-ocean model study, *J. Geophys. Res. Atmos.*, 120, 10,091–10,115, doi:10.1002/2015JD023386.

Received 17 MAR 2015

Accepted 5 SEP 2015

Accepted article online 11 SEP 2015

Published online 9 OCT 2015

Upper ocean response and feedback to spring weather over the Kuroshio in the East China Sea: A coupled atmosphere-ocean model study

Mien-Tze Kueh¹ and Pay-Liam Lin¹¹Department of Atmospheric Sciences, National Central University, Taoyuan, Taiwan

Abstract This study investigated the air-sea interaction over the Kuroshio in the East China Sea by focusing on the response and feedback of the ocean to typical spring weather events. The Weather Research and Forecasting Model was coupled with the HYbrid Coordinate Ocean Model for use in the study. The study period comprised a sequence of typical weathers in the area: prevailing southwesterly winds, the passage of a cold front and the ensuing cold-air outbreak, and the development of a Taiwan low. The air-sea interaction operated on a diurnal time scale under conditions of moderate wind speeds, high insolation, and a shallow oceanic mixed layer. The sea surface temperature and upper ocean heat content increased progressively prior to the frontal passage. The model reproduced the retreat of Kuroshio in response to the strong wind during the cold-air outbreak. The diurnal cycle vanished at high wind speeds. Wind stirring eroded the upper seasonal thermocline and deepened the oceanic mixed layer. The upper ocean heat content decreased because of entrainment cooling and surface heat losses. Surface restratification was subsequently suppressed in the thick and weakly stratified remnant layer. The consequently insufficient recovery of upper ocean heat content may have preconditioned a stagnation of the Taiwan low. The recovery of upper ocean heat content was discussed to derive the implication for climate simulations.

1. Introduction

The importance of warm sea surface temperatures (SSTs) along midlatitude western boundary currents in organizing clouds and precipitation has long been recognized [e.g., Xie *et al.*, 2002; Small *et al.*, 2008; Minobe *et al.*, 2008]. Most studies have observed the response of well-organized cloud belts or rain bands to warm currents on the basis of monthly or seasonal mean fields, which tend to mask the role of energetic transient weather systems in atmosphere-ocean coupling. During the winter-to-spring season, eastward passages of alternating synoptic-scale cyclones and anticyclones are commonly observed over East Asia. A propagating synoptic-scale cyclone typically travels with a southward stretching cold front across the region. The trailing cold front with an ensuing cold-air outbreak frequently swings through the East China Sea (ECS) [e.g., Nakada, 1991; Kato and Kodama, 1992]. The cold-air outbreak, being extremely cold and dry, can lead to unstable conditions when encountering warmer waters over the ECS. Vigorous surface heat and momentum fluxes associated with cold-air transformation can occur over the Kuroshio in the ECS [Kondo, 1976; Ninomiya, 1977]. These synoptic disturbances can precondition consequent subsynoptic-scale cyclogenesis, which is also commonly observed over the area. The warm Kuroshio is expected to facilitate the development of these subsynoptic-scale disturbances [Yu, 1980; Hanson and Long, 1985]. These subsynoptic-scale cyclones generally move northeastward into the North Pacific and can develop rapidly. The turbulent heat flux from the Kuroshio Current destabilizes the lower layer of the continental cold-air mass and releases latent heat, contributing to cyclone development [Chen and Dell'osso, 1987; Chen and Lu, 1997]. Shiota *et al.* [2011] indicated that the enhanced baroclinic zone along the Kuroshio Current provides favorable conditions for the rapid development of surface cyclones originating over the ECS. Chang *et al.* [1987] suggested that latent heat enhanced by regional baroclinic processes can result in explosive oceanic cyclogenesis. The role of synoptic- and subsynoptic-scale disturbances in regulating the air-sea interaction over the Kuroshio in the ECS (hereafter termed ECS Kuroshio) is crucial for the East Asian climate.

The Kuroshio carries warm and saline water from the tropics and enters the ECS after passing east of Taiwan. In winter and spring, the northward transport of the Kuroshio Current is often rendered by a warm tongue in the SST field over the eastern flank of the ECS. The development of intense precipitation and convective

©2015. The Authors.

This is an open access article under the terms of the Creative Commons Attribution-NonCommercial-NoDerivs License, which permits use and distribution in any medium, provided the original work is properly cited, the use is non-commercial and no modifications or adaptations are made.

clouds organized along the ECS Kuroshio have been studied by Xu *et al.* [2011] for late spring and by Sasaki *et al.* [2012] for early summer. Both studies have attempted to reveal the role of the Kuroshio in organizing deep convective precipitation by conducting regional model sensitivity experiments. The effect of the warm current on rainfall comes mostly from a modulating moisture supply that fuels the frontal system. All experiments were performed by prescribing SSTs in the model domains; therefore, a complete two-way air-sea interaction model is absent from their studies.

Distinct air-sea flux regimes have been documented for the passage of extratropical storms over waters [e.g., Bane and Osgood, 1989; Persson *et al.*, 2005]. During strong cold-air outbreaks, the Gulf Stream can be cooled by the large surface heat losses, and the ocean mixed layer (ML) can deepen by several tens of meters [Bane and Osgood, 1989; Xue *et al.*, 1995]. Strong winds can result in a shift of the Gulf Stream via the Ekman transport of upper waters [Xue *et al.*, 1995; Li *et al.*, 2002]. The ocean mixed layer depth (MLD) variability can modulate the efficiency of surface heat fluxes in regulating the upper ocean thermal structure, thereby preconditioning subsequent upper ocean variation [Kako and Kubota, 2007; Cronin *et al.*, 2013; Tozuka and Cronin, 2014]. The upper ocean dynamics is essential to the development of atmospheric cyclones [Yu and McPhaden, 2011; Seo and Xie, 2013; Jullien *et al.*, 2014]. In modeling, the representation of ocean ML dynamics is crucial for a wide spectrum of atmosphere-ocean couplings, for example, on diurnal cycles [Price *et al.*, 1986; Brainerd and Gregg, 1993b] and intraseasonal variability [Bernie *et al.*, 2005; Shinoda, 2005; Woolnough *et al.*, 2007]. The importance of the enhanced diurnal amplitudes in SSTs to climate variability has long been recognized [Bernie *et al.*, 2005; Shinoda, 2005; Kawai and Wada, 2007; Misra *et al.*, 2008; Kim and Hong, 2010].

The optical absorbance of upper waters serves as a critical contributor to diurnal signals in SSTs [Dickey and Simpson, 1983; Shinoda, 2005] and the mean state of ML stratification [Kara *et al.*, 2005a, 2005b]. In early regional coupled modeling studies performing summertime simulations of the Western Pacific, the ocean components have generally shown cool biases in SSTs [Ren and Qian, 2005; Fang *et al.*, 2010; Zou and Zhou, 2011]. The SST cool biases have been attributed to heat fluxes [Ren and Qian, 2005; Fang *et al.*, 2010] and cloud-solar interaction [Zou and Zhou, 2011]. However, these studies have not addressed the potential influence of upper ocean dynamics on the SST cool bias. Recently, Iwasaki *et al.* [2014] conducted a regional coupled modeling study on the coastal areas of the Yellow and East China Seas focusing on the variations of very near shore waters in winter. They discussed the response and feedback of the shallow coastal SSTs to the changes in the surface wind and upward heat flux. However, their coupling interval was set to 6 h which is insufficient for resolving a diurnal cycle. Mechanisms of upper ocean responses to atmospheric forcing and feedback from the ocean to the atmosphere vary depending on weather conditions. Knowledge of such responses and feedback is essential for identifying and reducing model biases in climate modeling systems.

This study examined the springtime air-sea interaction of the ECS Kuroshio under different weather conditions by using a regional atmosphere-ocean coupled model. The study period comprised a sequence of weather events frequently observed in the region. The response and feedback of the ocean to weather sequences were focused on to derive implications for climate simulations. Section 2 describes the models and the region of interest. Section 3 provides a synoptic description of the study period. Section 4 presents the coupled model results and examines the synoptic evolution, local variations, and surface heat fluxes in the model. Heat budget calculations to study upper ocean responses and an analysis of vertical structures are further presented in section 4. The model representations of upper ocean heat content and the implied effect on climate simulations are discussed in section 5. Section 6 presents a summary of the study.

2. Models, Region of Interest, and Data Description

The regional coupled modeling system consisted of models for the atmosphere and ocean, and a coupler for regridding and exchanging data fields. The atmospheric model used was the Weather Research and Forecasting (WRF) model with the Advanced Research WRF (ARW) dynamic core Version 3.4.1 [Skamarock *et al.*, 2008], and the ocean model component was the HYbrid Coordinate Ocean Model (HYCOM) Version 2.2.18 [Wallcraft *et al.*, 2009]. The coupler was implemented using the Spherical Coordinate Remapping and Interpolation Package (SCIP) [Jones, 2001] and the Model Coupling Environment Library (MCEL) [Bettencourt, 2002]. All the components are publicly available. The framework of the coupled model, the region of interest, and the data sets used are described as follows.

2.1. Atmosphere Component

The ARW is a compressible, nonhydrostatic mesoscale model formulated using a terrain-following mass vertical coordinate. The WRF modeling system implements a variety of physics options, initialization capabilities, boundary conditions, and grid-nesting techniques.

In this study, the WRF model was configured into a nested grid structure: a 45 km horizontal grid spacing domain over East Asia and a 15 km horizontal grid spacing domain centered on the ECS. The vertical grid structure consisted of 36 vertical levels, with 16 layers below 850 hPa over the ocean. The lowest level was placed approximately 14 m above ground or sea level. The parameterization choices used were identical for both grids: the new Kain-Fritsch cumulus scheme [Kain, 2004], the WRF Single-Moment 5-class microphysics scheme [Hong *et al.*, 2004], the Rapid Radiative Transfer Model for longwave calculation [Mlawer *et al.*, 1997], the Goddard shortwave radiation scheme [Chou and Suarez, 1994], the Yonsei University (YSU) planetary boundary layer (PBL) scheme [Hong *et al.*, 2006], the Unified Noah land surface model (Noah LSM) [Tewari *et al.*, 2004], and a surface layer scheme based on the Monin-Obukhov similarity theory. The fifth-generation Pennsylvania State University-National Center for Atmospheric Research Mesoscale Model surface layer (MM5-SL) scheme [Grell *et al.*, 1995, cf. section 5] was used for incorporating the YSU PBL scheme. The MM5-SL calculates surface fluxes, 10 m winds, and 2 m temperature and moisture. Over the ocean, the MM5-SL uses the sea surface skin temperature as the lower boundary condition for estimating surface fluxes, which can be prescribed using the SST derived from a data set or predicted by an ocean model. Over the lands, near-surface diagnostic variables and surface heat and moisture fluxes were updated by the Noah LSM.

The two domains were connected through a one-way nesting setup. For the outer domain, initial and lateral boundary conditions were obtained from the National Centers for Environmental Prediction (NCEP) Operational Global Final Analysis (FNL) data set. The daily global SST (RTG SST) analysis [Thiébaux *et al.*, 2003] used for lower boundary forcing was linearly interpolated to provide time-varying SSTs at 6 hour time intervals during our simulation period. The four-dimensional data assimilation technique implemented in the WRF was employed to perform three-dimensional analysis nudging [Stauffer and Seaman, 1990] on the coarse grid. Horizontal winds, temperature, and water vapor above the PBL were nudged toward the NCEP FNL fields over the course of model integration. Neither the analysis nudging nor any data assimilation of extra observations was incorporated during the integration of the inner domain. Only the finer grid was coupled to the ocean model.

2.2. Ocean Component

HYCOM is a community ocean model with a generalized vertical coordinate. This hybrid coordinate system allows for isopycnal coordinates in stratified oceans but uses the layered continuity equation to make a dynamically smooth transition to terrain-following coordinates in shallow coastal regions and to pressure coordinates (nearly fixed depth) in the ML and unstratified seas [Bleck, 2002]. The optimal coordinate is chosen every time step by using a hybrid coordinate generator. Further discussion and evaluation of the vertical coordinate in HYCOM can be found in Chassignet *et al.* [2003]. HYCOM implements several vertical mixing parameterizations; an evaluation of the performance of these schemes on the hybrid coordinate framework can be found in Halliwell [2004].

The HYCOM grid was configured with a horizontal resolution of 1/8°; the computational domain largely overlapped with the WRF inner grid (Figure 1a). The vertical discretization had 26 hybrid layers, with five upper layers of fixed depths to help resolve the ML. However, the thicknesses of these five upper layers could vary spatially. In deep water, the uppermost layer was set to 3 m, with the thickness gradually increasing with depth. The vertical coordinate was terrain following when the total depth of the water was shallower than approximately 130 m, and the top layer became progressively shallower until it was 0.5 m thick at the depth of 85 m. From there to the coast, the top layer remained 0.5 m thick. There were approximately five layers in the top 20 m for deep waters, whereas approximately 10 layers were used to resolve the top 20 m of shallow waters (with a depth of 50 m). The initial and lateral boundary conditions were derived from the HYCOM and Navy Coupled Ocean Data Assimilation (HYCOM/NCODA) global 1/12° analysis provided by the Naval Research Laboratory of the U.S. Navy. We used the daily snapshots of the HYCOM/NCODA on its native grid. The barotropic components were imposed using a lateral boundary technique described in Browning and Kreiss [1982]. The slow-varying baroclinic velocities, temperature, and salinity were nudged toward the given global data set in a buffer zone of five cells at the open boundaries.

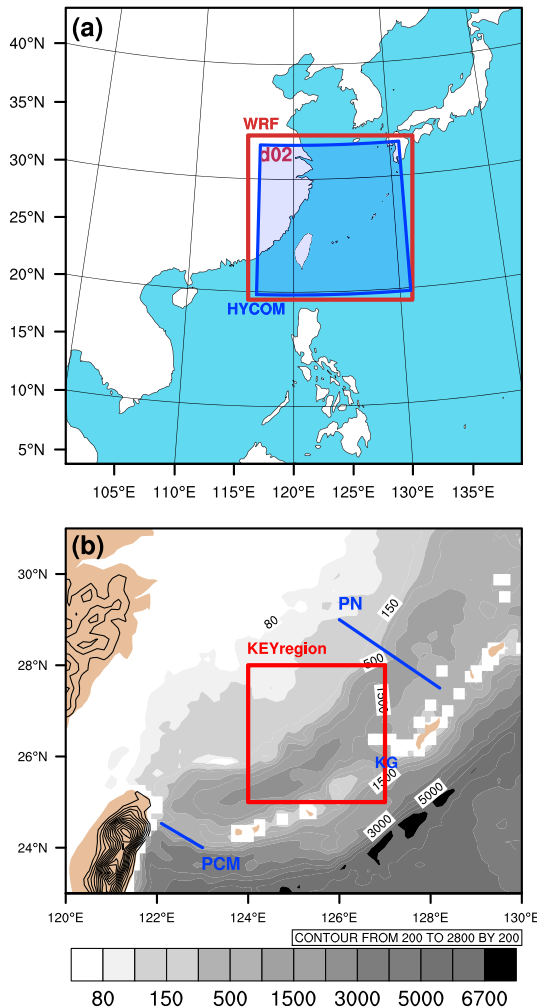


Figure 1. (a) The WRF outer domain with the finer domain (d02) and HYCOM domain enclosed by the inner brown and blue squares, respectively. (b) Topography used in the coupled simulation (a subregion of the full domain is shown). Red square encloses the key region. KG denotes the location of Kerama Gap. The blue lines (PN and PCM) correspond to the sections for transport calculations in Figure 10.

term includes the mean velocity difference from V_r and an unresolved turbulent velocity contribution to velocity shear. The variation of V_t depends on the combined effects of the turbulent and convective velocity scales under the constraint of the Monin-Obukhov similarity. In general, the turbulent velocity scale increases with friction velocity, whereas the convective velocity scale increases with surface buoyancy flux. Thus, V_t is essential in pure convection and other situations of little or no mean shear; additional details are provided in Large *et al.* [1994]. The surface turbulent boundary layer depth (SBLD) is estimated as the minimum value of d for which this bulk Richardson number exceeds a critical value (0.3 in our study). The variation in SBLD depends on the competing effects of buoyancy flux and wind stirring. At low wind speeds, an insolation-induced buoyant surface layer causes the SBLD to shoal. Strong winds generate velocity shear, which causes vertical mixing and a deepening of the SBLD. Evaporation, a strong function of wind strength, cools the surface and increases salinity, thereby inducing and enhancing convection, and causing variation in the SBLD through changes in buoyancy flux. The surface heat gains and losses are initially concentrated in the SBL because of the relatively strong eddy diffusivity but are then redistributed by dynamic processes. The large amount of heat gains and losses eventually contributes to temperature changes in the upper water column (the ML, mostly).

The nonlocal K-profile parameterization (KPP) [Large *et al.*, 1994] was applied as the vertical mixing scheme. In the KPP, a boundary layer depth is determined to address the distinct mixing processes in the surface boundary layer and interior. The surface boundary layer mixing accounts for the influences of wind-driven mixing, surface buoyancy fluxes, and convective instability. An additional nonlocal transport that permits counter gradient fluxes can enhance mixing where the surface boundary layer is unstable. In HYCOM, surface fluxes are evenly distributed over the uppermost model layer starting every time step, excluding penetrating solar radiation. Here the profile of solar penetration was computed following the Paulson and Simpson [1977] expression. The surface freshwater flux (i.e., evaporation minus precipitation) was treated with a virtual salt flux approach, which changes the salt content without changing mass.

The extent of the surface turbulent boundary layer (SBL) is determined on the basis of a bulk Richardson number:

$$R_{ib} = \frac{(B_r - B)d}{|V_r - V|^2 + V_t^2} \quad (1)$$

where d is the distance down from the surface, B is the buoyancy, and V is the mean horizontal velocity at depth d . B_r and V_r are the buoyancy and velocity at a near-surface reference depth, respectively. At a given depth d , the stabilizing mean buoyancy difference is computed relative to B_r , and the destabilizing shear

We adopted the SBLD to reveal immediate oceanic responses to atmospheric forcing and used a diagnostic MLD to inspect upper ocean dynamics as a whole. Because the MLD substantially depends on its definition, it can vary considerably from the SBLD determined in the KPP. Here the MLD was calculated as the first depth at which the potential density change with respect to the surface was an equivalent of 0.3°C; that is, the specified temperature change was converted to a local density change by using the equation of state before determining the corresponding depth. At runtime, the MLD was diagnosed using the prognostic temperature, salinity, and layer thickness after each time step. This means that the MLD aggregates the full ML dynamics and physical processes, including horizontal and vertical advects, diffusions, and diabatic heat sources.

2.3. Ocean-Atmosphere Coupling

At runtime, the two model components communicated and exchanged data via the coupler which was constructed using the SCRIP and MCEL. The SCRIP is a software package that computes addresses and weights for remapping and interpolating fields between grids in spherical coordinates. The MCEL is a set of libraries that handle the communication between different applications (i.e., the models) through the Common Object Request Broker Architecture. In the present study, the two models operated on different grid systems, and the atmosphere model ran on a grid (the inner one) with a larger spatial extent. The coupling fields from source grid to target grid were interpolated using the SCRIP. The atmosphere grid was adequately large to provide surface forcing for the ocean domain (Figure 1a). Because the ocean model could not provide a full spatial field of SST to the atmosphere model, the daily RTG SST used for the WRF outer domain was adopted to bridge the gaps proximate to the lateral boundaries. The WRF model provides 10 m surface winds, friction velocity, precipitation, surface evaporation, and radiative (shortwave and longwave) and turbulent (latent and sensible) heat fluxes at the surface. The total heat flux at the sea surface is defined as

$$Q_{\text{tot}} = Q_{\text{LH}} + Q_{\text{SH}} + (Q_{\text{LW}}^{\downarrow} - Q_{\text{LW}}^{\uparrow}) + Q_{\text{SW}} \quad (2)$$

where Q_{LH} and Q_{SH} represent the surface turbulent latent and sensible heat fluxes, and the remaining terms represent the radiative heat fluxes at the sea surface: the net longwave radiation ($Q_{\text{LW}}^{\downarrow} - Q_{\text{LW}}^{\uparrow}$, downward minus upward) and the net solar radiation (Q_{SW} , incident minus reflected). All surface fluxes are positive downward (into the ocean). Considering the absorbance of solar irradiance, the net heat flux absorbed from the sea surface down to depth z is defined as

$$Q_z = Q_{\text{surf}} + (Q_{\text{SW}} - Q_z^{\text{pen}}) \quad (3)$$

$$Q_{\text{surf}} = Q_{\text{tot}} - Q_{\text{SW}} \quad (4)$$

where Q_z^{pen} is the amount of solar irradiance that penetrates through the base of a water column at depth z , and Q_{surf} is defined as the Q_{tot} exclusive of Q_{SW} . Note that for HYCOM, the “surface” heat flux is the Q_z in the uppermost model layer; for example, it is $Q_z = 3$ when the top model layer is 3 m thick. In this context, HYCOM senses a net surface heat flux for which the penetrative solar radiation below the top layer is subtracted from the total heat flux. In this study, the solar penetration was computed using a two-band expression of exponential depth dependence:

$$Q_z^{\text{pen}} = Q_{\text{SW}} \left[R e^{-z/\beta_1} + (1 - R) e^{-z/\beta_2} \right] \quad (5)$$

where β_1 and β_2 are the attenuation lengths for the longwave (red) and the shortwave (blue-green) portions of the spectra, and R is an irradiance constant. These parameters are subject to water turbidity and have been specified empirically for various [Jerlov, 1976] water types by Paulson and Simpson [1977]. Preferential absorption of the longwave spectrum in the upper few meters is parameterized by the first term, whereas absorption of the shortwave spectrum below a depth of 10 m is parameterized by the second term. Our target was the Kuroshio, the strong current that flows from the Tropical Pacific. In the middle of the ocean, the sea water is clear and deep blue or almost black (meaning that little light is absorbed in the upper ocean); therefore, the strong Kuroshio Current, carrying clear water from the Tropical Pacific, is known as “the Black Current” in Japanese. In addition, Kuroshio in ECS is located in the subtropics, closer to the coasts and marginal seas where seawater contains more phytoplankton, which can absorb light. According to Jerlov [1976], the clearest water is classified as Type I, and Type IA represents clear coastal water with a higher attenuation than that of Type I. We chose Type IA for the entire domain.

The WRF model did not output wind stresses and upward longwave radiation at the sea surface. The coupler used the drag coefficient and 10 m winds provided by the MM5-SL to estimate surface wind stresses by using the standard bulk expression. The sea surface skin temperature on the WRF grid was applied to calculate the upward longwave radiation by using the Stefan-Boltzmann law for grey bodies. An emissivity of 0.98 was used in the coupler. The ocean model provided SST, which was taken as the water temperature of the top model layer, to the atmosphere model. In the coupler, the air-sea data exchange frequency is 1 h.

2.4. Region of Interest

The region of interest comprises portions of the continental shelf in the ECS and Okinawa Trough and is sufficiently far from the model boundaries (Figure 1b). The Okinawa Trough is a deep basin (in some cases deeper than 2000 m) following the continental shelf. The Ryukyu island chain separates the Okinawa Trough from the Philippine Sea (with depths of more than 5000 m) and acts as a barrier to deep water exchange between the two basins. The Kerama Gap, a deep channel that lies between the Okinawa and Miyako islands with a sill depth of approximately 1000 m and a maximum depth of approximately 1800 m, allows some water exchange through the Ryukyu island chain. We used the subarea enclosed by the red square in Figure 1b as the key region, which is occupied by the deep basin of the Okinawa Trough where the ECS Kuroshio flows and a portion of the shallow shelf with depths of 80–150 m. The Kerama Gap is proximate to the southeast corner.

The ECS Kuroshio is channeled by the shelf break and is bound to the east by the Ryukyu island chain. The main path and strength of the ECS Kuroshio exhibits a wide range of temporal variability. The major entrance for the Kuroshio to enter the ECS is at approximately 24°N, between the northeast coast of Taiwan and the southernmost portion of the Ryukyu Islands. Using historical observations at this entrance, the Kuroshio transport was estimated to be approximately 21 Sv (sverdrup, $1\text{Sv} = 10^6 \text{m}^3 \text{s}^{-1}$) with a range of variability of 10 Sv [Johns *et al.*, 2001; Lee *et al.*, 2001]; within the ECS, it is approximately 18 Sv with a variability range of slightly less than 10 Sv [Andres *et al.*, 2008a, 2008b]. Changes in the ECS Kuroshio transport may be caused by wind-driven variability in downstream transport [Ichikawa and Beardsley, 1993; Lee *et al.*, 2001] as well as the cross-stream Ekman displacement [Liu and Gan, 2012]. The arrival of mesoscale oceanic eddies from the east has long been recognized as contributing to the Kuroshio transport variability in the southern entrance to the ECS [e.g., Lee *et al.*, 2001] and through the Kerama Gap [Andres *et al.*, 2008a; Jin *et al.*, 2010].

2.5. Data Description

The following satellite and observational data sets were used in this study: (1) daily rainfall data from the Tropical Rainfall Measuring Mission (TRMM) Version-7 3B42 [Huffman *et al.*, 2007], (2) surface wind data from the Quick Scatterometer (QuikSCAT), (3) daily microwave and infrared optimally interpolated SSTs from the Multisensor Improved Sea Surface Temperatures (MISST) data set, (4) sea surface heat fluxes from the Objectively Analyzed Air-Sea Fluxes (OAFlux) [Yu and Weller, 2007; Yu *et al.*, 2008], (5) atmospheric fields from the NCEP Climate Forecast System Reanalysis (CFSR) [Saha *et al.*, 2010], and (6) historical Unidata Internet Data Distribution global observational data. The TRMM and QuikSCAT data sets are provided with a resolution of $0.25^\circ \times 0.25^\circ$. The MISST provides SST data with a finer resolution of approximately 9 km. The resolution of the CFSR reanalysis used here is $0.5^\circ \times 0.5^\circ$. The OAFlux data set is derived with a $1^\circ \times 1^\circ$ resolution.

3. Synoptic Overview of the Study Period

The study period was 0000 UTC 29 March to 0000 UTC 10 April 2007. In the span of 12 days, the study region experienced a sequence of weather events typical for the spring season. The study period can be divided into three stages according to the event sequence: prevailing southwesterly winds, the passage of a cold front and the ensuing cold-air outbreak, and the subsequent development of a subsynoptic disturbance.

1. *Stage I: Prevailing southwesterly winds (29–31 March).* Weather had been calm for the preceding 3 days. Figures 2a and 2g show the 3 day averages to illustrate the synoptic-scale picture. During the span of 3 days, southwesterly winds prevailed, with an eastward propagating continental high-pressure center to the north (outside the plotting domain) and a cold front trailing behind the center. The southwesterly winds carried warm and moist air over the warm Kuroshio waters. The cold front approached the coast by the afternoon of the third day.

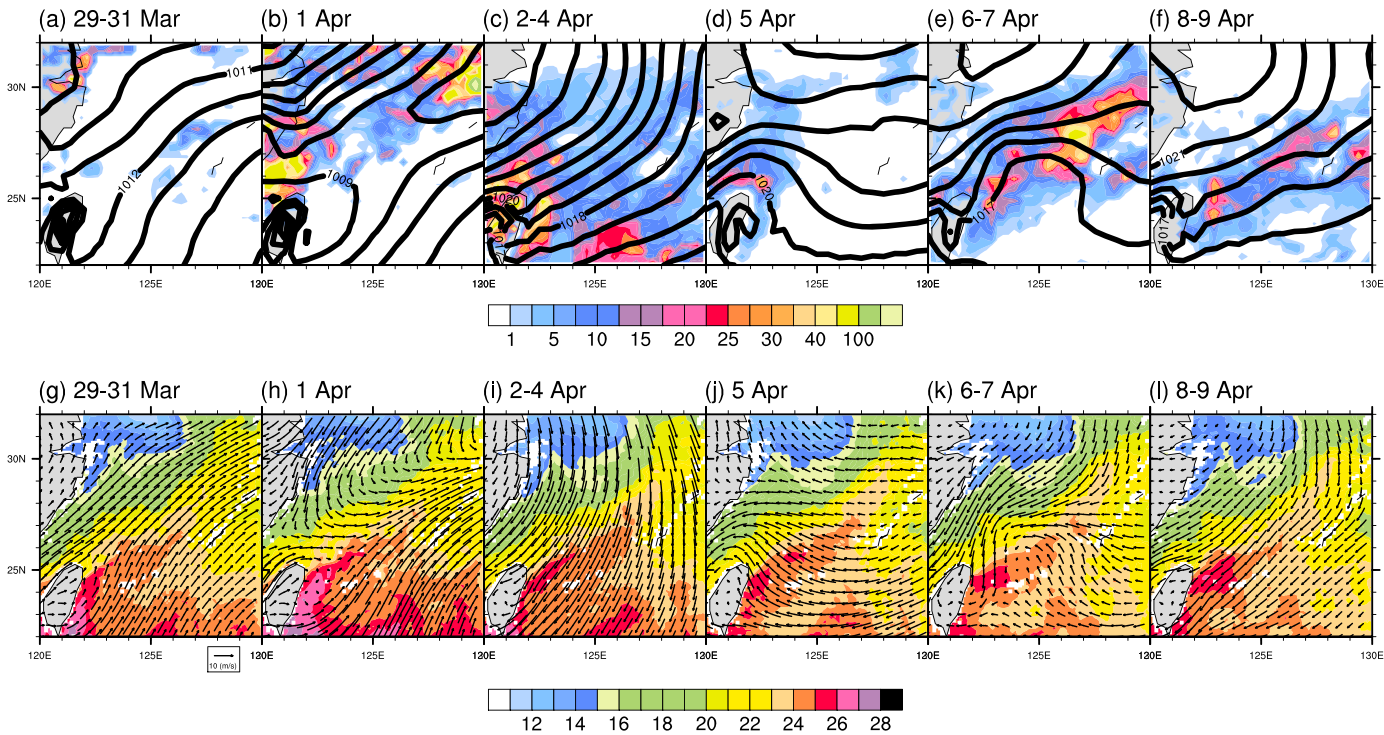


Figure 2. (a–f) The averages of mean sea-level pressure (hPa, contour) and precipitation rate (mm/d, shaded). (g–l) The averages of winds at 950 hPa (m/s, vector) and SST ($^{\circ}$ C, contour). From Figures 2a–2f and 2g–2l, the corresponding dates are 29–31 March, 1 April, 2–4 April, 5 April, 6–7 April, and 8–9 April. Note the differences in the time span for the averages. All fields are simply the temporal average of the corresponding dates, except that the precipitation rates are accumulated values. Mean sea-level pressure and winds at 950 hPa are derived from the CFSR 6-hourly data set. Precipitation rate and SST are taken from the daily TRMM 3B42 and MISST, respectively.

2. *Stage II: Frontal passage and cold-air outbreak (1–4 April).* The cold front, manifested by a surface pressure trough, moved progressively toward the key region on 1 April and produced heavy precipitation around the cyclone center to the northeast and over the northern Taiwan Strait to the southwest (Figure 2b). The front passed through the key region in the early morning of 2 April. Over the next 2 days, low-level north-northeasterly winds behind the front swept through the entire area bringing widespread precipitation, with relatively large amounts hitting Northern Taiwan and the warm waters farther south (Figure 2c). The warm Kuroshio waters made gradual progress northeastward with the southwesterly winds and then retreated under the influence of strong and persistent northeasterly wind bursts (Figures 2g–2i).
3. *Stage III: Taiwan low in ambient northeasterly winds (5–9 April).* On 5 April, the low-level flows turned east-southeasterly in association with an eastward propagating high-pressure center behind the frontal system (Figure 2d). A small low-pressure center formed within the precipitation area in the proximity of Northern Taiwan. The low center moved northeastward and developed into a cyclonic disturbance on 6 April and then moved slowly eastward to occupy the key region on 7 April (Figure 2e). This low center produced more precipitation over the ECS Kuroshio than the previous cold front did. Over the following 2 days, the low center moved off and the ECS was occupied by north-northeasterly winds (Figure 2f). This low center dissipated after a few days as it moved farther east. The warm Kuroshio has been speculated to facilitate the development of such subsynoptic disturbances commonly observed in this season [e.g., Yu, 1980; Hanson and Long, 1985]. Here we refer to it as the “Taiwan low” as in Yu [1980]. In this case, considering the gradual retreat of warm Kuroshio waters, the oceanic preconditions may have been unfavorable for the development of a Taiwan low.

Figure 3 presents a summary of the major features around the key region. The retreat of warm Kuroshio waters is evident from the SSTs within the sector of $124^{\circ}\text{--}126^{\circ}\text{E}$, where the Okinawa Trough resides (Figure 3a). The two precipitation episodes were accompanied with apparent southerly to northerly shifts in winds. Prior to the arrival of the frontal rain band, there was a net positive surface heat flux associated with low-negative surface turbulent heat fluxes (both latent and sensible heats were less than -50 W/m^2),

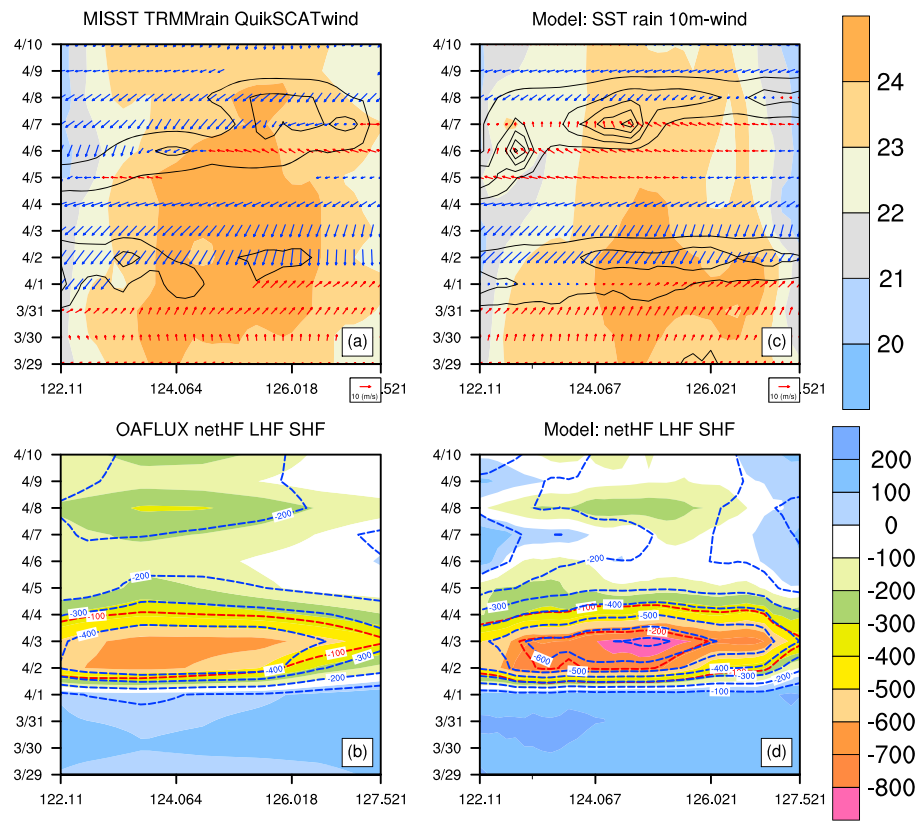


Figure 3. Time-longitude sections for daily (a) SST ($^{\circ}$ C, shaded), precipitation rate (mm/d, contour), and surface winds (m/s, vector), and (b) net surface heat flux (shaded), latent heat flux (blue contour), and sensible heat flux (red contour). All surface heat fluxes are in W/m^2 ; dashed lines indicate negative values. SST, precipitation rate, and winds are derived from MISST, TRMM 3b42, and QuikSCAT. Surface heat fluxes are from OAFLUX. (c and d) The same as Figures 3a and 3b, respectively, but for the coupled simulation. Note the different grid system for each data source. The sections are derived from a latitudinal sector of about 26° – 27° N.

suggesting a radiative heating on the ocean (Figure 3b). A reversal of the net surface heat flux from an oceanic gain to a loss occurred following the approach of the frontal rain band, indicating a heating of the atmosphere. The negative values of the surface heat fluxes (net and turbulent components) rapidly increased during the frontal passage (between 1 April and 2 April) and reached their peaks in association with the northeasterly wind burst, well after the passage of the cold front on 3 April. The contribution of the latent heat flux was obviously larger than that of the sensible heat flux. The high upward surface heat flux was probably less critical in producing intense frontal precipitation over the Kuroshio, compared with some previous studies that have emphasized the contribution of prefrontal upward heat fluxes [e.g., Xu *et al.*, 2011; Sasaki *et al.*, 2012]. The enhanced surface heat fluxes after the passage of the Taiwan low were apparently lower than those with the wind burst, probably because of the weaker cold air and relatively cooler water therein. Between the two episodes of stronger surface heat fluxes, the overall negative value of 100 – $200 \text{ W}/\text{m}^2$ was indicative of the oceanic contribution to the development of the Taiwan low.

4. Coupled Model Results

4.1. Synoptic Evolution

The model simulation was initialized at 0000 UTC 29 March and integrated for 12 days. The coupled simulation produced similar patterns of mean sea-level pressure and low-level winds as the CFSR reanalysis (Figure 4). The variations of precipitation and SST fields were also reasonably reproduced, although there were some discrepancies between the model simulation and observations. At Stage I, the coupled model produced marked wide-spreading precipitation over the region (Figure 4a). An inspection of the hourly output revealed that the coupled model produced a similar precipitation distribution on the first day and a rain-

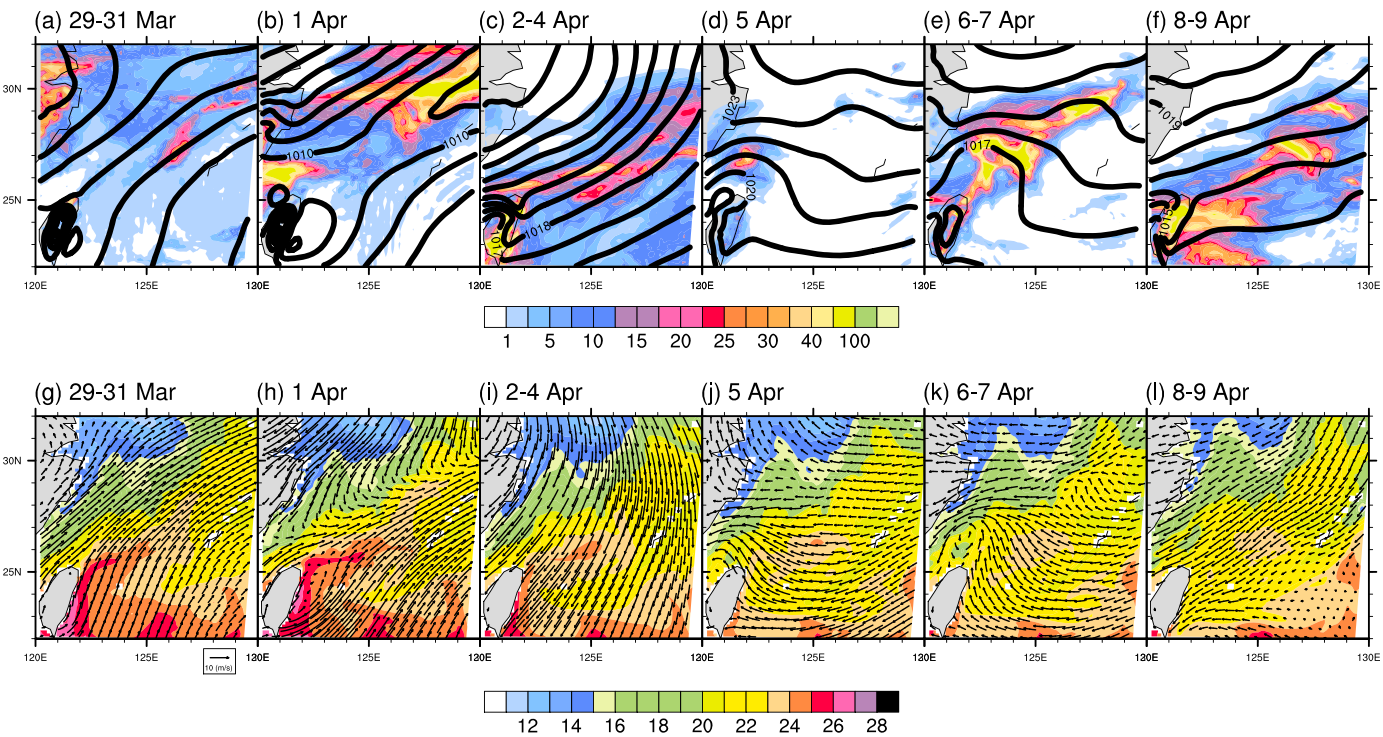


Figure 4. Same as in Figure 2 but for the coupled simulation.

free situation on the second day (figure not shown), as did the TRMM data set. However, the coupled model predicted a wide spread of light precipitation that accompanied the approaching cold front on the third day, which was absent in the TRMM data. This light precipitation was insignificant in the key region; thus, the bias is presumed to have less influence on the local air-sea interaction. The simulated cold front brought more intense precipitation along the Kuroshio (Figures 4b and 4c) and passed through the key region in the afternoon of 2 April, approximately 6 h behind that of the CFSR data set. The delayed frontal precipitation thus contributed to the precipitation distribution in the 2–4 April composite. The simulated Taiwan low formed on 5 April, but stayed longer over the shelf-water side, and gradually entered the key region in the nighttime of 7 April. It moved northeastward away from the Kuroshio around noon on 8 April, approximately 12 h behind that of the CFSR. The retreat of the warm Kuroshio waters was well reproduced in the first half of the entire period but was overestimated thereafter (Figures 4g–l). The degraded Kuroshio simulation could have been a cause of the model's stagnant development of the Taiwan low.

Although the coupled model produced more intense precipitation and surface heat fluxes, the similarities between the observed and simulated daily fields along the 26°N cross section reveal that it was reasonably good for demonstrating the synoptic evolutions over the study period (Figure 3). The simulated surface heat fluxes encountered rapid increases during the frontal passage and reached their peaks just after the passage of the front. Although the magnitudes of the simulated surface heat fluxes were considerably higher, their variations fairly resembled those presented in the OAFlux data set. The model produced weaker heat fluxes after the passage of the Taiwan low, and the surface heat fluxes during the development of the Taiwan low were lower than those in the OAFlux. This implies that the surface heat fluxes were insufficient for the development of the Taiwan low in the model. The degraded SST simulation for the second half of the study period is again evident in Figure 3.

Figure 5 shows the tracks of the Taiwan lows in the CFSR reanalysis and in the coupled simulation. The stagnant movement of the Taiwan low in the model is clearly shown. Figure 6 compares the model output with surface observations taken from nearby stations. The model output presented similar time evolutions to the observations and similar evolutions of vertical distributions compared with the upper air observations at two stations (Figure S1 in the supporting information). The modeled surface temperatures revealed significant diurnal variation; similar diurnal signals were found in station observations. At the marine stations, the diurnal

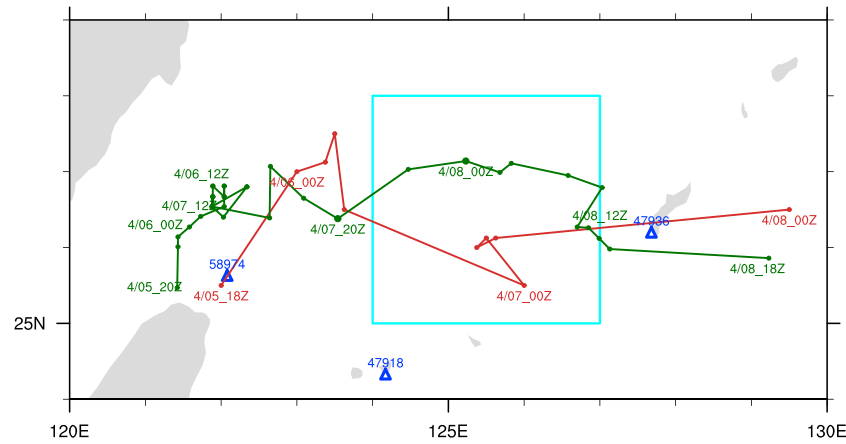


Figure 5. The tracks of the Taiwan lows in the CFSR (red, 6-hourly) and the coupled model simulation (green, 2-hourly). The locations of the Taiwan lows are determined by their central pressure, starting from 2000 UTC 5 April. Note the corresponding locations at 2000 UTC 7 April and 0000 UTC 8 April. Blue triangles denote the locations of three surface stations. Stations 47918 and 47936 also provide upper air observations. The cyan box is the key region.

amplitude of temperature did not present large differences prior to or after the cold-air outbreak. We followed the method in *Bernie et al. [2005]* to calculate the magnitude of the SST diurnal cycle: the difference between the daytime maximum of SST and the mean of the preceding and subsequent nocturnal minima. Prior to the cold-air outbreak, 12.9%–27.4% of grid points over the key region showed a high SST diurnal amplitude ($dSST > 0.5^{\circ}\text{C}$). The percentage of grid points showing $dSST > 0.5^{\circ}\text{C}$ was reduced to about 1.1%–6.5% during the cold-air burst and then increased again to approximately 10% after the burst. This analysis reveals a potential influence of synoptic conditions on SST diurnal variability in the model.

4.2. Local Variations

Atmospheric and oceanic surface variations in the key region fairly well demonstrated the synoptic evolution (Figure 7). The surface pressure increased slightly with the eastward propagating high-pressure center prior

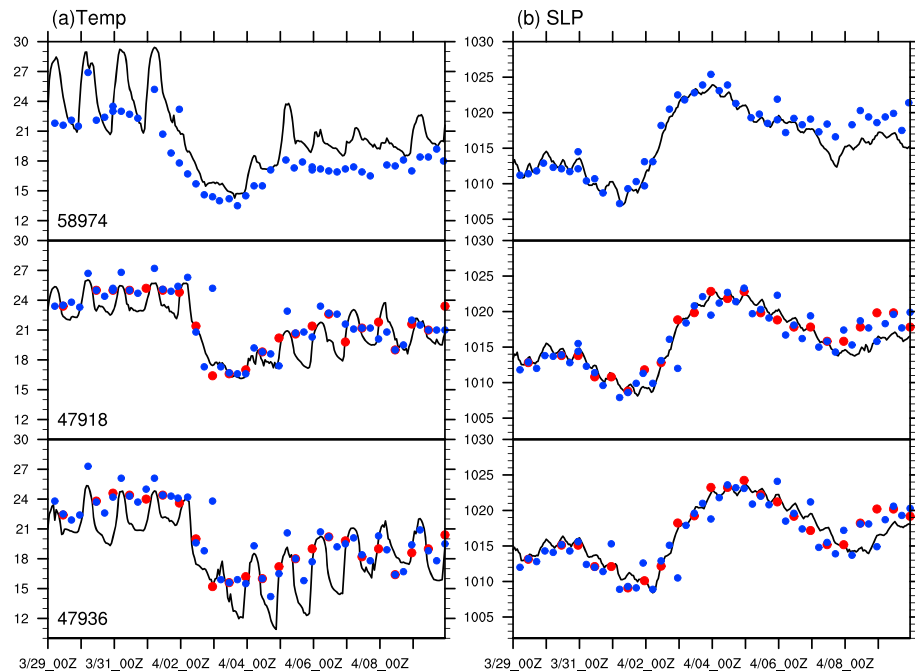


Figure 6. Time series of (a) surface temperature and (b) mean sea-level pressure (SLP) taken from the three surface stations denoted in Figure 5 (blue dots) and derived from the model output (black lines). The model data are taken from the nearest land points upon the three station locations. Red dots are data from the upper air observations.

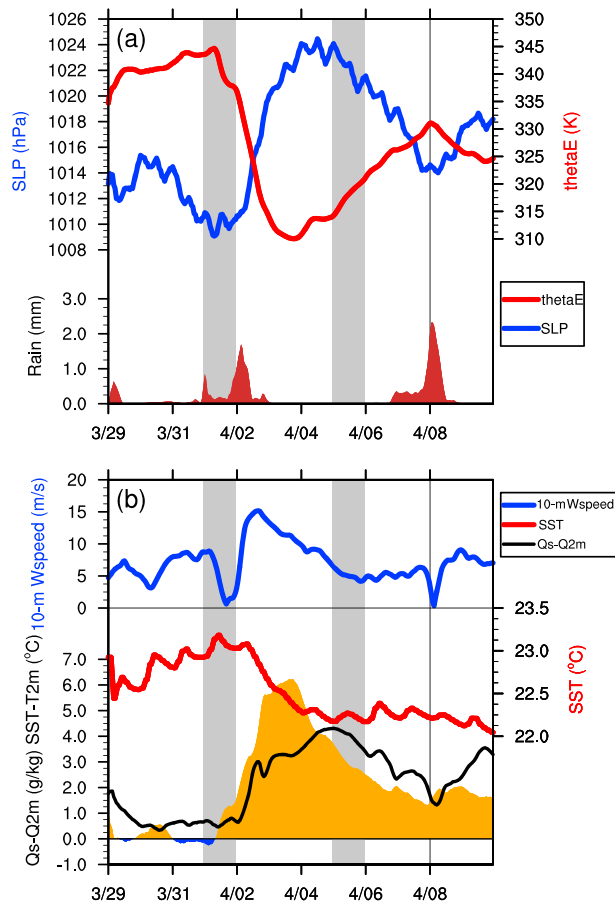


Figure 7. Time series of the modeled output averaged over the key region for (a) mean sea-level pressure (hPa, blue), equivalent potential temperature (K, red), and precipitation amount (mm; hatched), and (b) wind speed at 10 m (m/s), SST ($^{\circ}$ C, red), air-sea moisture gradient ($Q_s - Q_{2m}$; g/kg, black) and temperature gradient (SST – T_{2m} ; $^{\circ}$ C, hatched). Q_s and Q_{2m} are water vapor mixing ratio at sea surface (saturated) and at 2 m, respectively. T_{2m} is air temperature at 2 m. The two grey vertical bars indicate the time spans of 24 h on 1 and 5 April, respectively, the black vertical line denotes 0000 UTC 8 April.

contrasts) changed in response to atmospheric and oceanic variations. The air-sea thermal contrasts were low with spells of negative temperature gradients observed during Stage I. Following the northeasterly wind burst, drastic increases in air-sea thermal contrasts of up to 6° C and 4 g/kg occurred within a few days. They gradually decreased but remained relatively high during Stage III. The SST and surface θ_e experienced similar trends during the first two stages; however, their variations were different at the third stage. On a synoptic time scale, air-sea thermal contrasts depend substantially on the variability of near-surface atmospheric states. The SST exhibited apparent diurnal oscillations with moderate wind speeds, which were also shown in the air temperature at 2 m (figure not shown). The diurnal signals in both temperature fields vanished at high wind speeds. Because near-surface wind speeds and air-sea thermal contrasts are essential to surface flux estimations, the air-sea interaction during our study period was expected to operate on various time scales.

4.3. Surface Fluxes

Diurnal cycle of the total surface heat flux (Q_{tot} , equation (2)) was evident over the entire period (Figure 8a). The behaviors of the diurnal cycle exhibited strong dependence on the synoptic evolution. In general, Q_{tot} was positive during the day and negative during the night, except for the daytime of 3 April. The radiative and turbulent components of the surface heat fluxes varied greatly with the weather conditions. Solar

to the cold front and then dropped with the frontal passage. The ensuing continental high led to a drastic increase of approximately 14 hPa in 2 days. The surface pressure then underwent a gradual drop until it reached a second minimum around 8 April, demonstrating the development of the Taiwan low. In general, a relatively high surface pressure is associated with the prevalence of northeasterly winds (cf. Figure 3). The near-surface equivalent potential temperature (θ_e at 2 m) gradually increased with the warm and moist southwesterly flow and then dropped drastically with the cold and dry northeasterly burst. At Stage III, the moderate rise of the surface θ_e revealed the warm and moist air supply for developing the Taiwan low; however, the overall values were well below that of Stage I because of the ambient northeasterly winds. The cold-air outbreak resulted in strong near-surface winds with a maximum wind speed of up to 15 m/s over the key region. Prior to and after this wind burst, moderate wind speeds of around 5–8 m/s occupied the region. The two precipitation episodes occurred with a relatively high θ_e and extremely short spells of wind speed approaching zero. The SST increased steadily at a rate of 0.5° C per 3 days during the southwesterly stage. It dropped drastically by 0.7° C over 2 days during the wind burst and remained cool thereafter irrespective of the decrease in wind speed.

The air-sea temperature and specific humidity differences (hereafter termed as thermal

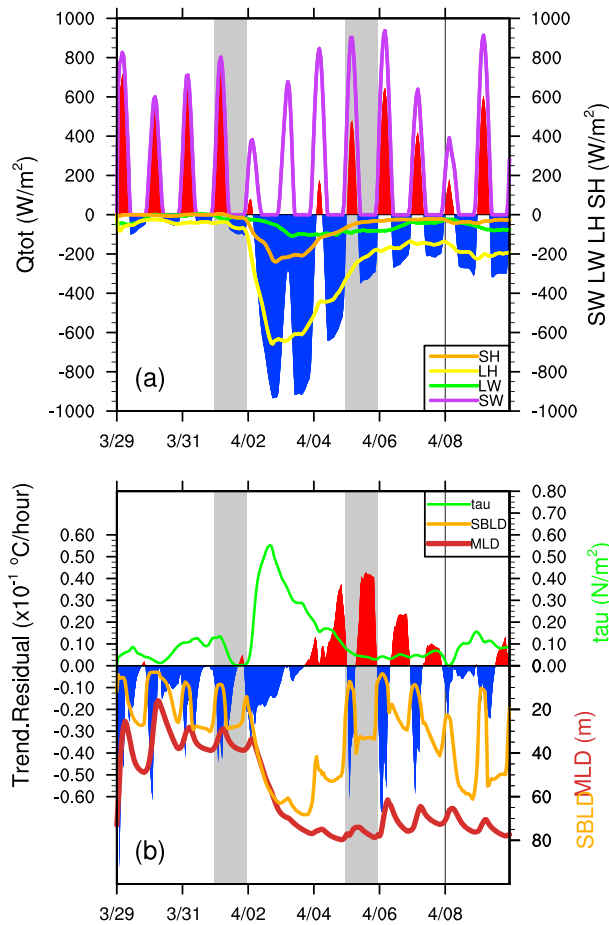


Figure 8. Time series of the modeled output averaged over the key region for (a) surface heat fluxes: net solar radiation (SW), net longwave radiation (LW), latent heat (LH), sensible heat (SH), and total heat flux (hatched), and (b) surface wind stress (N/m^2), SBLD (m), MLD (m), and residual ($\times 10^{-1} \text{ }^{\circ}\text{C/h}$, hatched). All surface heat fluxes are in W/m^2 . The grey vertical bars and black vertical line denote time spans as in Figure 7.

drastically to as high as -650 W m^{-2} and -250 W m^{-2} , respectively. The revived solar heating after the cold front was insufficient to compensate for the turbulent heat loss, resulting in a substantially negative Q_{tot} over time. At Stage III, the turbulent heat losses gradually decreased, partially offset solar heating and maintained a relatively large nighttime cooling.

The relationship between the changes in surface forcing and SSTs is not altogether straightforward. The SST experienced large diurnal oscillations when wind speeds were moderate and insolation was high. Recurrent insolation led to an increasing SST trend in the course of a few days. The decreasing SST trend coincided with the wind burst, demonstrating the wind-driven cooling effect. The evaporative heat loss associated with the violent air burst was efficient in cooling the waters. At Stage III, the SST did not return to its preburst values, despite the daytime heating being comparable to that of the first stage. Therefore, in addition to surface forcing, the varying upper ocean structure plays a role in regulating SST changes.

4.4. Upper Ocean Response

Variations in the SBLD and MLD depended substantially on the surface forcing over most of the study period; diurnal signals in both the SBLD and MLD were found except when the wind stirring was excessively strong (Figure 8b). Marked changes in the SBLD and MLD were noted during the three stages. The SBLD and MLD remained mostly in the upper 40 m at Stage I and subsequently plunged to a depth of below 60 m during

radiation dominated daytime heating but varied from less than 400 W m^{-2} during cloudy and rainy spells to greater than 800 W m^{-2} in clear weather. Net longwave radiation is generally low and negative, acting to cool the ocean, because the downward component is typically overcome by several tens of watts per square meter from sea surface longwave emissions. In our case, the downward component displayed a variability of $20\text{--}60 \text{ W m}^{-2}$ in a day, in contrast to the upward component varying by $1\text{--}5 \text{ W m}^{-2}$. Therefore, the slightly enhanced net longwave radiative cooling during the high-wind and cool-SST stages can be ascribed to a reduction in the downward component caused by decreased cloudiness and the cold and dry boundary layer air. The change in turbulent heat fluxes (latent and sensible heat) is responsible for shaping the synoptic variability of Q_{tot} . During the frontal passage, increased cloudiness blocked a significant amount of solar radiation. The frontal precipitation and enhanced wind resulted in depleted daytime heating and a substantial surface heat loss over time. The reduced solar heating was further offset by a turbulent heat loss, leading to a depletion of daytime Q_{tot} . The northeasterly wind burst brought cold and dry air over the warm Kuroshio, causing vigorous air-sea thermal contrasts. Both the surface latent and sensible heat fluxes grew

substantially exceeded their preburst

values. The revived solar heating after the cold front was insufficient to compensate for the turbulent heat

loss, resulting in a substantially negative Q_{tot} over time. At Stage III, the turbulent heat losses gradually

decreased, partially offset solar heating and maintained a relatively large nighttime cooling.

the first half of Stage II. Their trends separated thereafter, with the SBLD gradually shoaling and the MLD remaining deep. The preexisting MLD was generally deeper than the SBLD, which meant that surface forcing almost always embedded the SBL in a weakly stratified water column. We term the portion of the ambient ML that is capped by the SBLD as the remnant layer.

Stage I was characterized by strong insolation, moderate wind speeds, and extremely weak nocturnal cooling. Insolation-induced surface stratification caused a shallow SBLD in the daytime, often with depths of less than 10 m. Moderate winds and weak surface cooling prevented the SBLD from deepening substantially in the nighttime. The MLD closely followed the SBLD, with a maximum nocturnal depth of approximately 40 m, slightly deeper than that of the SBLD. Strong winds and surface cooling produced a sharp deepening of the SBLD and MLD. From the afternoon to midnight (for approximately 11 h) on 2 April, the SBLD was slightly deeper than the MLD, suggesting an entrainment of cooler water from below. As the wind and surface cooling weakened, the SBLD became shallow, manifesting a surface restratification process. However, the MLD remained at a depth mostly below 60 m, leading to a thick remnant layer. When the MLD trend separated from that of the SBLD, the diurnal fluctuation of the MLD became less sensitive to surface forcing. This sluggish response to surface forcing was largely due to the thick remnant layer, which damped the diurnal signal in the MLD owing to the large thermal inertia.

SST variation in the key region generally followed the trend of the MLD throughout the study period (Figures 7b and 8b). To isolate the effect of surface forcing on subdaily SST variability, we related the hourly tendency of simulated SST to the imposing atmospheric heat flux by using a surface boundary layer heat budget expression:

$$\frac{\partial \text{SST}}{\partial t} = \frac{Q_{z=\text{SBLD}}}{\rho_w c_{pw} \text{SBLD}} + \text{residual} \quad (6)$$

where ρ_w and c_{pw} are the density and specific heat capacity, respectively, of seawater. SBLD is defined in equation (1), and $Q_{z=\text{SBLD}}$ is the net heat flux absorbed from the sea surface down to the base of the SBL (equation (3)). *Residual* includes all other oceanic processes: horizontal and vertical advection, entrainment, and diffusion. The first term on the right-hand side of equation (6) is an effective heat flux (Q_{eff}) or the amount of $Q_{z=\text{SBLD}}$ as scaled by the SBLD. In this context, the simplest thermodynamic relation for the upper ocean is that the change rate of SSTs can be mostly balanced by Q_{eff} , but this is valid only when the residual is near zero. Using the *Paulson and Simpson* [1977] expression with the *Jerlov IA* water type, the absorbed solar radiation over a depth of 3 m (10 m) is expected to be approximately 67% (77%) of the net solar radiation at the surface (Q_{SW}); the proportion that can reach deeper waters (for example, beyond 20 m) is approximately 13% of Q_{SW} . The warming of the water column below the SBL or the ambient ML caused by this penetrating irradiance is not negligible [e.g., *Dickey and Simpson*, 1983; *Kara et al.*, 2005a, 2005b]; this heat can be released back to upper layers during subsequent deepening of SBL and/or ML.

The SST tendency and Q_{eff} were calculated using 1-hourly model output fields at each grid. The amount of solar radiation that penetrated through the base of the SBL, $Q_{z=\text{SBLD}}^{\text{pen}}$ from equation (6), was calculated using the 1-hourly SBLD, although this changed with every time step. The reversal of the sign of Q_{eff} mostly corresponds to that of Q_{tot} (the total heat flux shown in Figure 8a). The timing of the reversal of the SST tendency generally coincided with that of Q_{eff} ; over the study period, the exact time lag between the two never exceeded 3 h. The time series of the SST tendency, Q_{eff} , and residual are depicted in Figure S2 in the supporting information. We present only the residual here and refer to the positive (negative) value as residual warming (cooling). For a positive SST tendency rate that occurred mostly in the daytime, a residual cooling indicates a dampening effect of oceanic processes on the warming rate caused by surface heating. For a negative SST tendency rate, a residual cooling means that the amount of heat loss from the sea surface is inadequate to account for the SST drop, and as such, a further mechanism is needed to cool the water layer. A residual warming, however, indicates that oceanic processes provide supplemental heat, preventing the SST from excessive cooling and further sustaining the surface heat loss.

Apparent diurnal SST variability was found prior to and after the cold-air outbreak. We take 29–31 March and 5–7 April as examples. Daytime residual cooling was found for these days irrespective of the depths of the ambient ML. However, nocturnal residual cooling and warming were found along with the relatively shallow and deep ambient MLD, respectively. Residual cooling occurred during the cold-air outbreak. On the basis of

the diurnal behaviors of the residual, we concentrated on three major oceanic mechanisms responsible for modulating the surface contribution to the subdaily SST tendency. We attempted to interpret the residual from a vertical perspective. Because of the variant water depths and the existence of the Kuroshio, the upper ocean response to atmospheric forcing is not expected to be uniform throughout the key region. The upper ocean dynamics and effect of Kuroshio variations on ambient stratification are described in a subsequent section.

In the apparent diurnal cycle, eddy diffusive mixing likely contributed substantially to daytime residual cooling. At low wind speeds, the insolation-induced positive buoyancy flux restricted the depth at which near-surface turbulence could penetrate; hence, most of the incoming heat was trapped near the surface, increasing the SST. This surface restratification process was manifested in the formation of a diurnal warm layer consisting of a considerably thin surface ML with a diurnal thermocline underneath. Although turbulent exchange with the ambient water below would have been damped by the stable thermal stratification of the diurnal thermocline, a nonzero diffusivity, mostly caused by shear instability, could have vertically transmitted heat away from the SBL. The source of the shear instability was the near-surface diurnal inertial jet. This mixing process dampens the SBL warming rate expected by Q_{eff} . Because the remnant layer below the base of the SBL is often weakly stratified, diffusive mixing can further transfer the incoming heat downward to potentially increase the heat content. Notably, the structure of the diurnal warm layer can exert influence on the following nocturnal SST cooling because of the amount of trapped heat therein.

During the first spell of diurnal cycles, namely 29–31 March, the MLD was relatively shallow. A close inspection revealed that the daytime residual cooling decreased as the positive SST tendency rate diminished in the evening, and then the nighttime residual cooling began to increase when the SST tendency rate turned negative (see Figure S2). Different oceanic processes were responsible for this nighttime residual cooling, which occurred largely only during the first few hours and was then significantly reduced. At the low-wind stage, a shallow diurnal warm layer generally formed well before noon and was then eroded by eddy diffusion over time. As solar heating was overcome by surface heat losses, convection further eroded the diurnal warm layer into a deeper layer of well-mixed water temperatures. Heat stored near the surface mixed downward, causing the SST to cool without necessarily increasing the amount of surface heat loss. This redistribution of the daytime heat gain contributed to a large nighttime residual cooling in the earlier hours around sunset. A further SST drop would have required a substantial amount of heat loss after the full erosion of the diurnal warm layer. Wind speeds were relatively low and the surface heat loss was significantly small during this stage; hence, mechanical and convective mixing could only penetrate to a limited depth and may have only caused a weak entrainment cooling to contribute to the residual. Thus, a predawn decreasing residual cooling was found.

For the diurnal cycles following the strong wind burst, the ambient ML was relatively deep. The diurnal thermocline was weak or hardly found because of the high ambient diffusivity; the diurnal warm layer was ill-defined or no longer discernible within the markedly weaker ambient stratification. In the daytime, less heat was trapped near the surface, whereas the nocturnal surface heat loss was large because of the strong air-sea thermal contrast. The destabilizing surface heat loss coupled with wind-induced turbulence caused the nocturnal SBLD to deepen and to vertically redistribute the daytime heat gain. However, both diurnal warm layer erosion and entrainment cooling were unlikely to have effectively contributed to the SST change because residual warming occurred at this time. An additional heat supply was necessary to compensate for the surface heat loss. The deep ambient ML, or more specifically the thick remnant layer, was capable of retaining more daytime heating, because more incoming heat into the SBL was diffusively transmitted downward and a larger proportion of solar irradiance was expected to be absorbed by the thick layer. This absorbed heat below the SBL can further weaken the ambient stratification and act to dampen the cooling rate of the upper layer in response to any subsequent mixing, because relatively warm water is then entrained. In this context, the engulfment of relatively warm water from below was expected to alleviate the SST drop and sustain the large surface heat loss, thereby contributing to nighttime residual warming. Notably, a lateral heat supply can also modulate the ambient stratification.

The diurnal signal was suppressed during the cold-air outbreak, namely from the evening of 2 April to midnight of 3 April. Although there was a large amount of surface heat loss, the cooling efficiency was degraded subject to the vigorous deepening of the SBLD caused by convective mixing and wind stirring.

Consequently, the heat lost from the surface was inadequate to account for the considerable SST drop. Because the SBLD was slightly deeper than the MLD here, the entrainment of cooler water from below the base of the ambient ML was expected to further cool the water layer, thereby contributing to residual cooling. The weakening of the wind burst was associated with residual warming. At this time, the insolation-induced surface restratification (i.e., diurnal warm layer formation) could cause the SST to rise, yet the SBLD was still sufficiently deep to cause the surface incoming heat flux to approach zero in the SBL budget expression (equation (6)), resulting in a positive daytime residual. The nighttime residual warming could be interpreted as that in the diurnal cycle following the wind burst. The northeasterly winds and surface cooling were slightly enhanced after the passage of the Taiwan low. The deep ambient ML maintained a rather weak background stratification to facilitate deep penetration of the SBL, driven by a relatively weak wind (in comparison to the wind burst). At this time, the downward diffusive transfer of surface heat gains and entrainment cooling contributed to the daytime and nighttime residual cooling, respectively.

The response of the ECS Kuroshio to the cold-air outbreak was appreciably rendered by the retreat of the warm SST tongue both in observations and in simulation. This corresponded with a sharp SST drop over the key region. Any diurnal signals in air-sea interaction operated in association with this synoptic SST fluctuation. Although no attempt was made to isolate the contribution of lateral heat advection to the residuals, we could not completely rule out the role of the time-varying Kuroshio in modulating the upper ocean stratification. Therefore, we further calculated the heat budget of the ML. The flux form of the heat budget in the ML can be expressed as [see, e.g., *Caniaux and Planton, 1998*]

$$\rho_w c_{pw} h \partial_t \langle T \rangle = \rho_w c_{pw} \left[-h \langle U \rangle \cdot \nabla \langle T \rangle - \nabla \int_{-h}^0 \widetilde{U} \widetilde{T} dz \right. \\ \left. - [\langle T \rangle - T(h)] w_e(-h) + \overline{w' T'}(-h) + h A_H \nabla^2 \langle T \rangle \right] + Q_{z=ML} \quad (7)$$

where $\rho_w c_{pw}$ is the volumetric heat capacity of seawater, T is the water temperature, U is the horizontal velocity with (u, v) as the eastward and northward components, w is the vertical velocity, h is the MLD, A_H is the horizontal eddy diffusivity, and $Q_{z=ML}$ is the net heat flux absorbed from the sea surface down to the base of the ML (equation(3)). The vertical average of any variable a over the ML is defined as $\langle a \rangle = \frac{1}{h} \int_0^h a dz$, and the deviation from this average is defined as $\tilde{a} = a - \langle a \rangle$. The entrainment velocity is defined as $w_e(-h) = w(-h) + \partial_z h + U(-h) \cdot \nabla h - A_H \nabla^2 h$. The left-hand side of equation (7) is the heat storage. The individual terms in the right-hand side, from left to right, are the horizontal advection of heat by the depth-averaged current, the advection by the deviations of this mean current, the entrainment heat flux at the ML base, the vertical turbulent mixing at the ML base, the horizontal heat diffusion, and the net heat flux absorbed in the ML.

The heat budget was evaluated using the 1-hourly model output over the key region. Because of the wider variation in the water depths over the key region, we separated the water column into shallow (<500 m) and deep (>500 m) for analysis. The result reveals that a combination of horizontal heat advection, entrainment heat flux, and net absorbed heat flux could explain most of the heat storage changes in our case. These terms are shown in Figure 9. In addition to the apparent heat loss during the cold-air outbreak stage, heat storage in the ML showed significant diurnal variations. In general, the net absorbed heat flux and entrainment heat flux contributed to daytime increases and nighttime decreases in heat storage, respectively. Over the shallow waters, both net absorbed heat flux and entrainment heat flux contributed to heat loss in the ML, whereas positive horizontal heat advection acted to supply heat to the water layers. By contrast, the positive contribution of horizontal heat advection over deep waters appeared to decrease during the cold-air outbreak. Therefore, we expected that some warm Kuroshio waters could be transported shoreward to supply heat to the shelf waters, under the control of the strong cold-air burst.

4.5. Evolution of Vertical Structures

To infer the bulk of Kuroshio strength variability, we estimated the downstream transport of Kuroshio (VT_k) as an analogy to the definition demonstrated by *Ichikawa and Beardsley [1993]*:

$$VT_k = \frac{1}{\rho_w g} \int_{L_E}^{L_W} \int_{-D}^0 V_n dz dL \quad (8)$$

where ρ_w is density of sea water, g is gravity, and V_n is the downstream (positive value) baroclinic velocity normal to the cross-section bound by locations L_W and L_E . The depth D is 300 m or the entire water column, whichever is shallower. We estimated the Kuroshio transport across the two sections shown in Figure 1. The

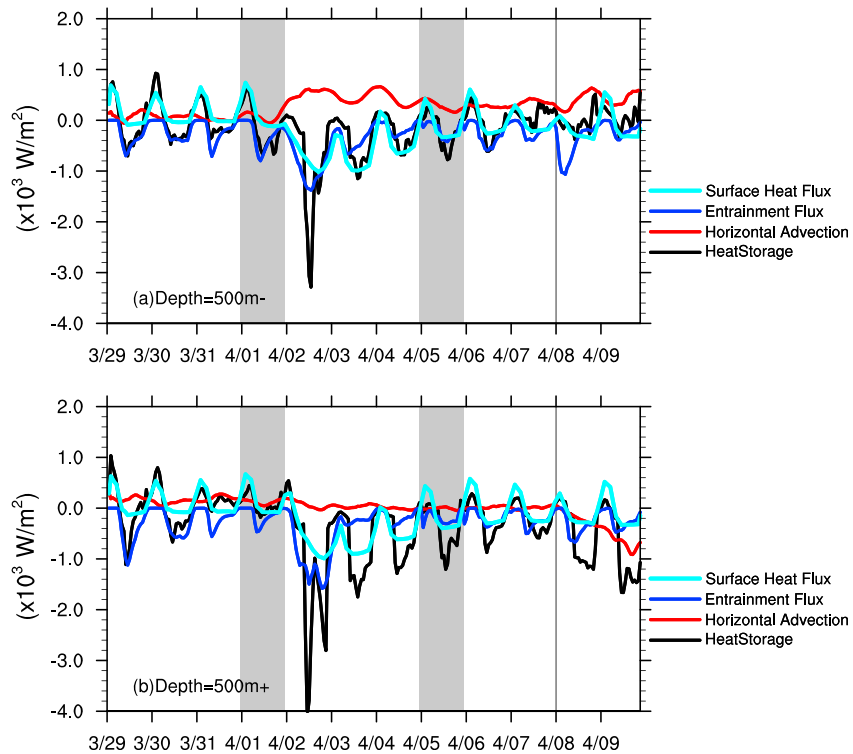


Figure 9. The ML heat budget averaged over the (a) shallow and (b) deep waters. The shallow and deep represent waters depths of $< 500 \text{ m}$ and $> 500 \text{ m}$, respectively, within the key region. Only the heat storage, horizontal advection, entrainment flux, and surface heat flux are shown. All terms are in W/m^2 . The grey vertical bars and black vertical line denote time spans as in Figure 7.

mean transport of the study period was approximately 14.6 Sv and 12.8 Sv for the downstream (PN) and upstream (PCM) sections, respectively, of the key region (Figure 10); both values were within the ranges of variability derived from observations (cf. section 2.4). The PN transport was larger than the PCM transport at

Stage I. Both the northward shelf current originating from the Taiwan Strait and the net inflow through the Kerama Gap could have contributed to the PN transport. Both the PN and PCM transports were sensitive to wind stirring, having decreased following the strong wind burst. The PCM transport rebounded to approximately 15 Sv after the wind burst had diminished, whereas the PN transport remained at a low value of approximately 10 Sv . This was interpreted as an accumulation of Kuroshio inflows within the ECS during the development of the Taiwan low. After the passage of the Taiwan low, the further decreases in the PCM and PN transports corresponded to a degraded SST simulation.

The atmospheric and oceanic boundary layers underwent apparent changes during the cold-air outbreak. Prior to the cold front, a thick layer of southwesterly

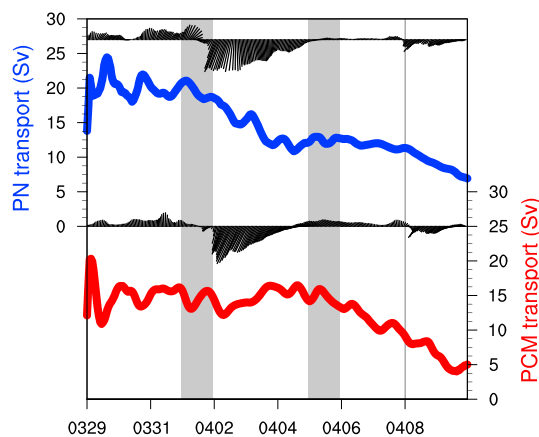


Figure 10. Kuroshio downstream transport derived from the transect lines PCM (red) and PN (blue). Wind sticks denote the corresponding surface wind stresses (N/m^2) and are oriented in the direction the wind is blowing to, with true north is straight up. The line PCM (PN) nearly coincides with the hydrographic survey section PCM-1 (PN-line). The PCM-1 is a moored instrument array east of Taiwan deployed during the World Ocean Circulation Experiment [Johns et al., 2001]. The PN-line is a repeat survey section west of Okinawa [cf. Andres et al., 2008b]. The grey vertical bars and black vertical line denote time spans as in Figure 7.

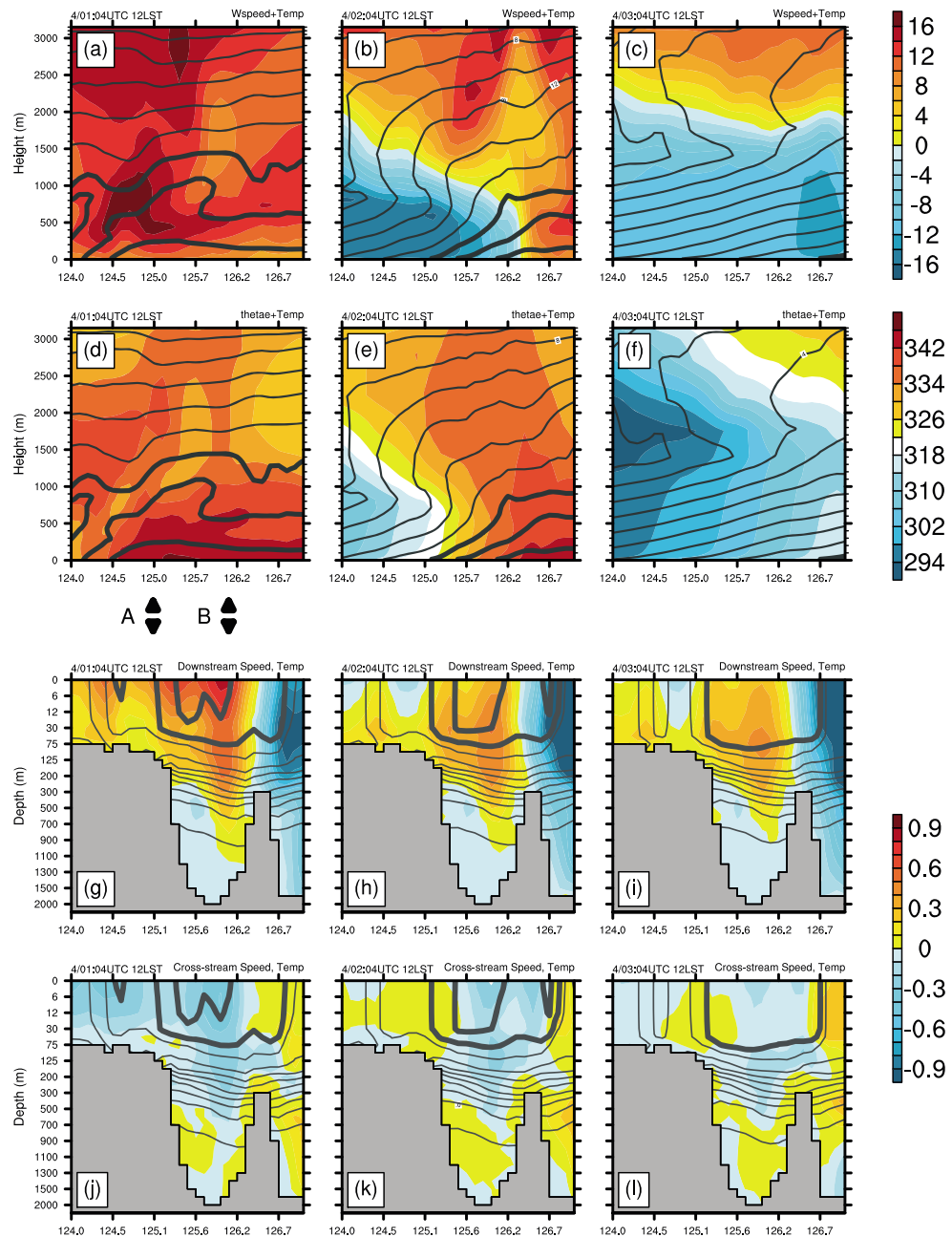


Figure 11. Cross sections derived along the northwest-southeast diagonal of key region. Vertical structures of (a–c) normal wind speed (m/s) and (d–f) equivalent potential temperature (K) are superimposed by air temperature ($^{\circ}\text{C}$, contour), and (g–i) downstream and (j–l) cross-stream ocean velocities (m/s) are superimposed by ocean temperature ($^{\circ}\text{C}$, contour). From Figures 11a–11c, 11d–11f, 11g–11i, and 11j–11l, the corresponding dates are from 1 to 3 April. For Figures 11a–11f, thick contours represent air temperature above 18°C . For Figures 11g–11l, thick contours represent ocean temperature above 23°C . Both the winds and currents are rotated 45° anticlockwise, so that positive values represent velocity component normal (into the page; southwesterly/downstream) or tangent (toward left; shoreward) to the section. Triangles A and B, in proximity to shelf break and Kuroshio core, respectively, indicate the locations of plots in Figures 12 and 13.

winds rendered the lower atmosphere warm and moist (Figures 11a and 11d). The upward decreasing θ_e suggested an unstable stratification in the surface layer. Following the northeasterly winds behind the cold front, the retreat of warm air temperatures and the intrusion of low θ_e values were manifestations of the cold-air outbreak (Figures 11b, 11c, 11e, and 11f). The vertical gradient of θ_e diminished significantly, manifesting a release of lower atmospheric instability. The ECS Kuroshio together with the shelf flows exhibited a

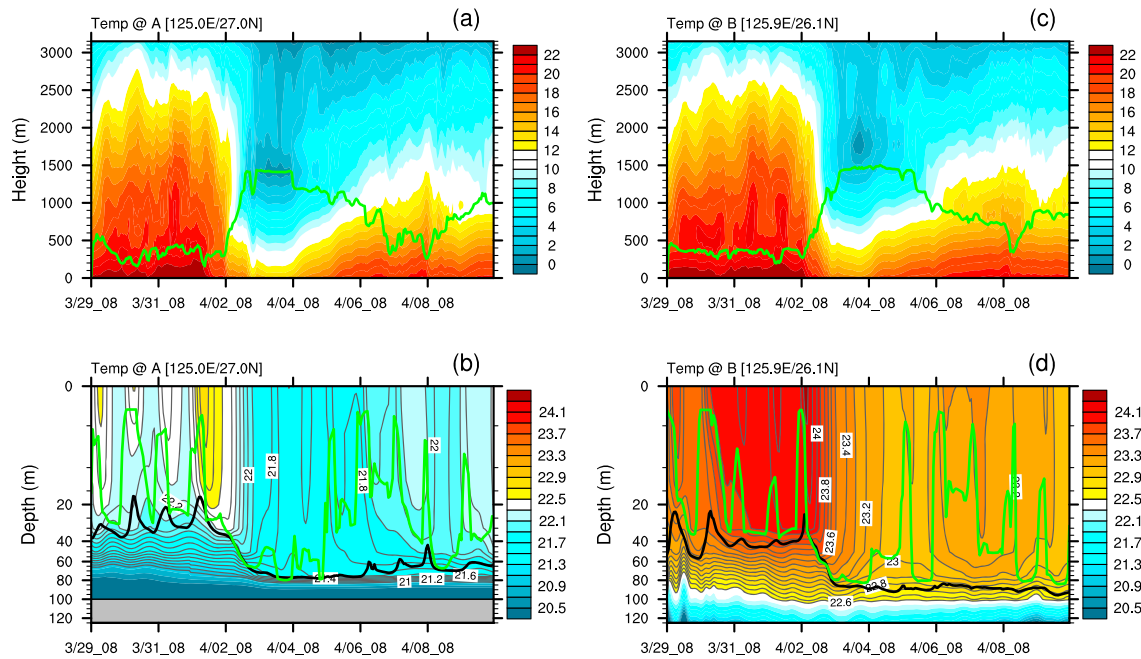


Figure 12. Time series of vertical structure derived at A for (a) air temperature ($^{\circ}$ C) and (b) ocean temperature ($^{\circ}$ C). The corresponding PBLH, SBLD, and MLD are also plotted. (c and d) The same as Figures 12a and 12b, respectively, but are taken from B. Locations A and B are marked in Figure 11.

multicore structure of downstream velocity components (Figure 11g). The multicore flow structure of the ECS Kuroshio Current system has been recognized in other studies [e.g., Andres *et al.*, 2008b]. Under the strong northeasterly winds, the Kuroshio and shelf flows decelerated along with the descent of the downstream velocity cores (Figures 11h and 11i). Over the shelf break, the occurrence of onshore water displacement was presumably Ekman drift, driven by the wind as opposed to the near-surface current (Figures 11j–11l). Above the seasonal thermocline, the water layer was cooled with the reduced Kuroshio. Notably, a cyclonic eddy existed southeast of the Kerama Gap throughout the study period, leading to a southward flow over the eastern edge of the cross section. This eddy contributed to a weak net inflow to the ECS through the Kerama Gap, in analogy with the flow pattern recognized by Jin *et al.* [2010]. The weakening of the ECS Kuroshio's strength corresponded to a decrease in the PN transport, whereas the onshore displacement may have retained more warm waters over the outer shelf. This corresponded to the Kuroshio inflow accumulation noted in Figure 10. After the passage of the Taiwan low, the onshore displacement was enhanced (figure not shown), thereby contributing to the further reduction in the PN transport.

A number of spatial inhomogeneities were evident over the key region, in particular on the ocean side. Figure 12 illustrates the time evolution of the temperature profiles from two locations in proximity to the shelf break and the core of Kuroshio. The atmospheric and oceanic vertical thermal structures at both locations consistently presented distinct regimes corresponding to the three synoptic stages. The cold-air outbreak, characterized by substantial cooling throughout the lower atmospheric columns and upper ocean layers, separated the prior and posterior regimes. In response to the energetic synoptic event, a vigorous exchange of surface fluxes between the atmosphere and ocean led to a significant thickening of the boundary layers (PBL and SBL) on both sides. Both sides of the boundary layer thicknesses decreased following the weakening of the wind burst. The MLD, however, remained deep, thereby separating from the SBLD, as previously noted. The deepening of the MLD corresponded to the erosion of the upper seasonal thermocline, leading to vigorous entrainment cooling of the upper waters.

Diurnal coupling signals between the atmosphere and ocean were evident during the prior regime. The lower atmospheric warm layers, which can extend up to 2.5 km, revealed a wave-like structure fluctuating roughly on a diurnal time scale (Figures 12a and 12c). In proximity to the shelf break, the oceanic ML exhibited daytime downward penetrating dome-like warm patches, demonstrating the development and erosion of diurnal thermoclines (Figure 12b). Because of the daytime ML shoaling, the effect of wind stirring (i.e., the

momentum flux) was largely trapped near the sea surface and thus enhanced the near-surface current speed. This could also be seen in the diurnal signal of the Kuroshio transport. Consequently, dome-like structures of velocity also coincided with these warm patches (figure not shown), forming a stratified shear flow at the diurnal thermocline. This strong shear instability could have induced eddy diffusive mixing despite the stable thermal stratification. The increasing thickness of the diurnal thermocline (i.e., the downward penetrating warm patch) over the daytime could be attributed to the downward heat transferred by the shear-driven eddy diffusive mixing [Price *et al.*, 1986; Brainerd and Gregg, 1993a, 1993b] and could also be partially contributed to by penetrated solar heating near the base of the diurnal thermocline [Brainerd and Gregg, 1993b]. The wave-like disturbance in the upper seasonal thermocline manifested the combination of daytime penetrating solar heating and nocturnal entrainment cooling. Over the Kuroshio core, the considerably weaker dome-like structure and wave-like disturbance may have been due to the relatively weak ambient ML stratification and deep thermocline (Figure 12d). On 30 March, there was a substantial warming of the ambient ML. This resulted from a lateral heat convergence caused by the Kuroshio flow field. However, this was not apparent in the area-averaged ML heat budget analysis (Figure 9b). We therefore calculated the full budget terms over the water column at this location, and the result showed a significant horizontal heat advection on 30 March (Figure S3 in the supporting information). This warming was not found over the shelf break. However, a sudden warming occurred on 1 April, which was caused by the combined effect of solar heating and a short period of confluent northward currents in the upper 30 m depth just before the arrival of the cold front (see Figure S4 for the local heat budget). At both locations, the penetrating depth of the diurnal thermocline continued to deepen slightly during this stage, suggesting a gradual increase in the surface-driven warming of the water column. The upper ocean heat content increased over time (will be shown later). The daytime heating rate greatly exceeded the nighttime cooling rate during this stage; therefore, although the erosion of the diurnal warm layer could have caused the SST to drop, further cooling of the water layer would have required additional mixing processes [Dickey and Simpson, 1983; Shinoda, 2005]. From a vertical perspective, the enhanced daytime stability and suppressed nocturnal mixing could contribute to the increase in the upper ocean heat content over time [e.g., Dickey and Simpson, 1983].

The time lag between the arrival of the wind burst at the two locations was demonstrated by the different timings for the diminished near-surface warm air (see the isotherms above 21°C). The time lag was even evident on the ocean side, as revealed by the nearly isothermal layer in the ML. The diminished stratification in the upper seasonal thermocline corresponded to the overall cooling of the ML because of wind stirring. Strong wind stirring occurred after the formation of the diurnal warm layer in the Kuroshio core on 2 April, approximately 8 h behind the burst over the shelf break. After the strong burst, the recovering surface warm air layers were relatively thin and gradually extended upward with the development of the Taiwan low, but never returned to the preburst level. The oceanic MLs were thick and less stratified, and the diurnal surface restratifications were less evident at both locations. The diurnal signals in the seasonal thermocline were also ambiguous because solar heating and turbulent mixing were less influential at the ML base. The thick remnant layer acted to decouple the ocean beneath from the diurnally varying surface boundary layer, leading to a less fluctuating seasonal thermocline. The accumulation of Kuroshio inflow, noted in Figure 10, corresponded to the warming of the upper water columns during the Taiwan low development. The northeasterly winds strengthened slightly following the passage of the low and the warming of the upper waters over the Kuroshio core diminished, but warming over the shelf break continued to increase for the rest of the simulation. This shelf break water warming was primarily caused by the Ekman-driven onshore displacement of Kuroshio waters. Overall, lateral heat supply was likely effective in compensating for the surface heat loss, but the causes of the change in heat supply were different over time.

Figure 13 presents a summary of the major oceanic responses discussed in this study. Under light wind conditions, a shallow surface warm layer was produced by stratified solar heating (Figures 13a and 13d). The diurnal warm layer overlaid the weak stratified ambient water layer, which is a remnant of the previous night's ML. A portion of the incoming heat was diffusively transmitted downward, causing the diurnal thermocline to thicken over time. For small surface heat losses, the vertical redistribution of heat caused by the full erosion of the warm layer was responsible for the nocturnal SST drop. Further cooling required the entrainment of cooler water from below, but it was limited (Figure 13a). This nocturnal cooling of the upper water layer could be alleviated or even overwhelmed by a lateral heat transport, which could also change the ambient stratification as well as the upper ocean heat content (Figure 13d). On the arrival of

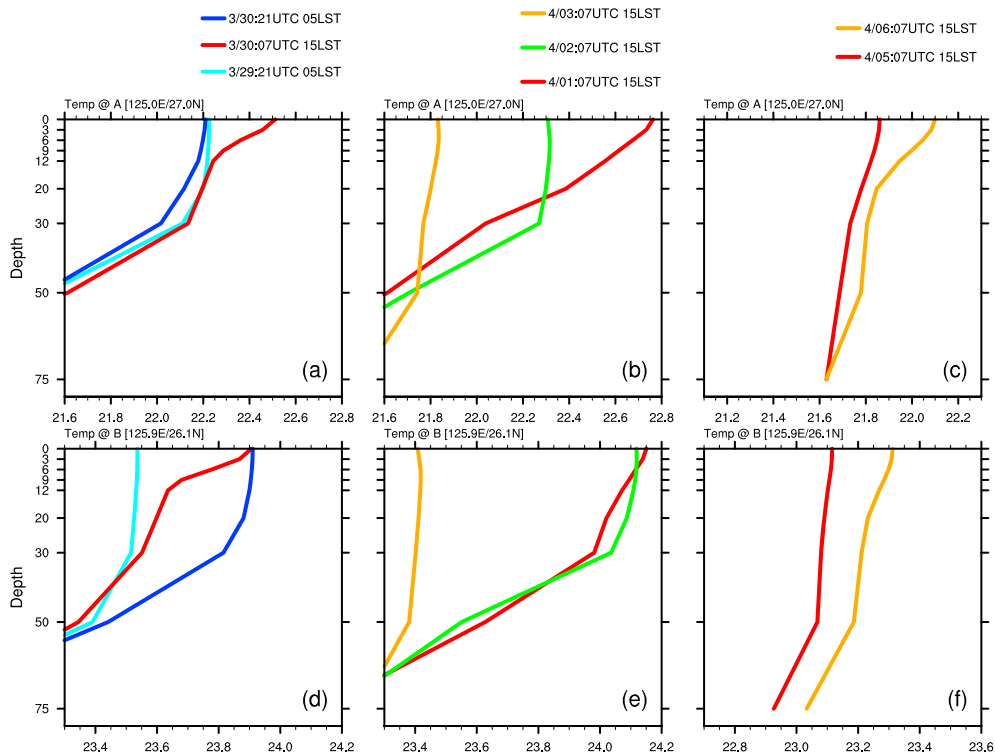


Figure 13. Vertical profiles of ocean temperature ($^{\circ}$ C) taken from locations A and B. (a–c) for A and (d–f) for B. Note the leftward shift in the transverse scales of Figures 13c and 13f. Locations A and B are marked in Figure 11. The profiles are taken at 0500 and/or 1500 local time on selected days in the three stages (see legend).

the wind burst, the deepening of the nearly well-mixed layer along with the near-surface unstable temperature gradient could occur even during the daytime (Figures 13b and 13c). The SST diurnal cycle vanished because the high wind speed generated sufficient vertical mixing to destroy any surface stratification. The wind-driven vertical mixing entrained cooler, sublayer water up from below, eroded the upper seasonal thermocline, and deepened the ML. Cooling throughout the upper water column manifested a loss of upper ocean heat content, which was primarily determined by the amount of heat loss from the surface and entrained cool water; the SST dropped accordingly. The strong wind stirring left behind a markedly deeper, cooler, and less stratified remnant layer, which enable more heat to be diffusively transmitted downward, such that less heat would be trapped to form a diurnal warm layer (Figures 13c and 13f). The diurnal response was generally confined to the upper 15 m depth. The thick remnant layer could have presumably facilitated additional penetrated solar radiation to be absorbed in the deep ML and acted to decouple the surface boundary layer from the cooler water beneath. Additional lateral heat supply could have contributed to the warming of upper waters. These heat sources could have maintained a weak ambient stratification and sustained the local surface heat loss. Because the temperatures of the upper water columns were substantially lower than their preburst values, a considerably longer period of insulation or additional lateral heat supply would have been necessary to reestablish the upper ocean heat content (e.g., back to the preburst amount) in such a thick remnant layer.

5. Upper Ocean Heat Content and Surface Restratiification

The insufficient recovery of modeled heat content may have caused an inadequate energy supply for the development of the Taiwan low. To infer the bulk of the change in the upper ocean thermal state, we calculated the columnar upper ocean heat content in proximity to the two locations by vertically integrating the temperature over a water layer between the surface and a specified depth H (m):

$$HC = \rho_w c_{pw} \int_0^H T_z dz \quad (9)$$

where $\rho_w c_{pw}$ is the volumetric heat capacity of seawater and T_z is the depth-dependent temperature. The changes in ocean heat content of the water column above 100 m are a good measure of the oceanic response

for the various stages, because it includes both ML cooling and upper seasonal thermocline heating. We first calculated the hourly heat content in the upper 100 m and then inspected the daily average to infer the synoptic evolution. The hourly heat content and SST presented similar trends throughout the study period.

Prior to the frontal passage, the shelf break and Kuroshio core experienced a heat content gain of approximately 80 MJ m^{-2} and 177 MJ m^{-2} , respectively, in 4 days. For the shelf break, approximately 50% of the heat gain occurred from 31 March to 1 April, in response to the sudden warming of the water column noted in Figure 12b. Over the Kuroshio, the heat content increased gradually starting on 30 March, indicative of the Kuroshio heat supply. Surface heat gain was also a contributor to the increase in heat content. The prefrontal peak values of the shelf break and Kuroshio core were 8.9 GJ m^{-2} and 9.6 GJ m^{-2} , respectively. The difference between the heat content amounts at the two locations could exceed 700 MJ m^{-2} , demonstrating the potential energy supply of the Kuroshio for the atmosphere. Strong wind stirring caused a loss of the upper ocean heat content in the region. In the span of 3 days, the heat content decreased by nearly 210 MJ m^{-2} over the Kuroshio core, whereas the amount of heat loss over the shelf break was small ($\sim 50 \text{ MJ m}^{-2}$). This is because the shelf break water could gain heat from wind-driven onshore water displacement. Both locations underwent a reestablishment of heat content (up to 73 MJ m^{-2}) approximately 2 days prior to the arrival of the Taiwan low, in response to the enhanced insolation as well as the accumulation of Kuroshio warm waters over the region. Following the passage of the Taiwan low, a heat content loss (gain) occurred over the Kuroshio (shelf break) amounting to 63 MJ m^{-2} (48 MJ m^{-2}) in 2 days, demonstrating the consequences of the second period of onshore water displacement.

During the second half of the study period, the Kuroshio experienced a great decrease in heat content because of the vast amounts of surface and lateral heat loss. The amount of surface heat gain or loss, the entrainment of waters from below, and advective effects are the primary factors for determining the magnitude of changes in upper ocean heat content [e.g., Dickey and Simpson, 1983; Large *et al.*, 1994; Cronin *et al.*, 2013]. Cronin *et al.* [2013] suggested that the rebuilding of the seasonal thermocline occurs first through horizontal processes and then through solar radiative heating. This is because advection-induced sublayer restratification can cause the ML to be shallow, thereby intensifying surface warming and restratification through the reduction in effective thermal inertia. Regarding the surface ML (with a depth of a few tens of meters), penetrating solar insolation can account for approximately 60% of observed restratification, whereas lateral advection can supply most of the rest [Brainerd and Gregg, 1993b; Hosegood *et al.*, 2008]. In the Northern Hemisphere, the spring season manifests an upper ocean restratification stage after a long spell of strong wind stirring in winter. This seasonal restratification can thereby precondition the consequent recovery of upper ocean heat content because the relatively shallow ML facilitates the retaining of more heat. In our case, over the short span of a few days, the solar heating and lateral heat advection were apparently insufficient to reestablish the upper ocean heat content over the Kuroshio to its preburst amount. The consequent disturbed period of the Taiwan low was also unfavorable for surface restratification. A longer integration is necessary to confirm if there is eventually a modulation of mean coupled climate for this region by temporal variability of the upper ocean heat content in response to spring weather disturbances and to quantify the model shift arising from the representation of the upper ocean thermal structure.

To assess the sensitivity of the Taiwan low development to changes in the SST, we performed additional experiments by using fixed SST fields starting at different times in the coupled simulation. For example, a fixed SST experiment starting from 0000 UTC 2 April was a WRF-only simulation, in which we fixed the SST field for the rest of the integration period. Five experiments with fixed SSTs starting from 0000 UTC of 1 April to 5 April were performed; each represented a different SST value during Stage II (cf. Figure 7b). These hybrid experiments (coupled and fixed SSTs) allowed for an identical synoptic evolution prior to the frontal passage and prescribed different SST fields during and/or after the cold-air outbreak. We attempted to present the influence of the preconditioning SST on the development of the Taiwan low. Experiments fixed-0401 and fixed-0404 were similar to fixed-0402 and fixed-0405, respectively. Thus, only three experiments (fixed-0402, fixed-0403, and fixed-0405) are shown. All the experiments captured the deepening phase and diurnal variation (Figure 14). In addition, warmer SSTs resulted in a stronger low-pressure center, namely with a deeper central sea-level pressure. A stronger low-pressure center accompanied faster and more straightforward movement. In all experiments, relatively large latent and sensible heat fluxes were found to the south and east of the low-pressure centers (Figures S5 and S6 in the supporting information). We calculated the area average of surface latent and sensible heat fluxes prior to and during the development of the Taiwan low in these experiments (Table S1 in the supporting

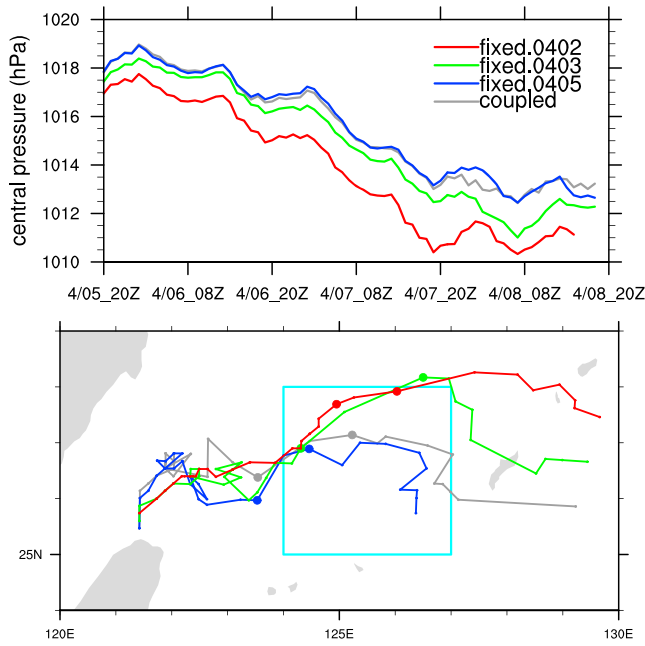


Figure 14. (top) Time series of the central sea-level pressures and (bottom) tracks of the Taiwan lows. The 2-hourly locations of the Taiwan lows are determined by their central pressure, starting from 2000 UTC 5 April. For each experiment, the two solid circles denote the locations at 2000 UTC 7 April and 0000 UTC 8 April, respectively.

the solar spectrum [Shinoda, 2005]. At present, there is little knowledge of the optical properties in this region. Using the *Paulson and Simpson* [1977] expression with the *Jerlov IA* water type, an attenuation length of 0.6 m was specified for red light, such that a greater proportion would have absorbed in a few tens of centimeters from the surface. However, our top model layer over deep waters was 3 m; the profile of optical absorbance in the upper few meters was indeed ill-resolved. In reality, the diurnal warm layer can be confined to above the 1 m depth under weak wind conditions (cf. the review in *Kawai and Wada* [2007]). The diurnal SST amplitude in our simulation may have a low bias because of the inadequate vertical resolution, contributing to the bias in the surface flux calculation.

6. Summary

The springtime air-sea interaction over the Kuroshio in the ECS under various synoptic conditions was studied. The response and feedback of the upper ocean to atmospheric forcing were focused on to derive their implications for climate simulations. The WRF model was coupled with the HYCOM for use in the study. The study period comprised a sequence of weather events typical during the spring season in the region. To distinguish the air-sea interaction on different synoptic conditions, the study period was divided into three stages according to the weather events in sequence: prevailing southwesterly winds, the passage of a cold front and the ensuing cold-air outbreak, and the subsequent development of a Taiwan low.

Vigorous heat loss from the ocean surface and gradual retreat of the warm Kuroshio waters were observed following the cold-air outbreak, manifesting the ocean's response to the strong wind burst. The oceanic supply of heat and moisture contributed to the development of the Taiwan low, although the contribution may have been limited because of the retreat of the Kuroshio and the relatively cool SST after strong wind stirring. The coupled model properly reproduced the synoptic evolution. The passage of the cold front and the ensuing cold-air outbreak was captured. On analysis of the surface fluxes and upper ocean dynamics, the major upper ocean response and feedback to this sequence of weather events can be summarized as follows.

Under the conditions of moderate wind speeds and strong insolation, the interaction between the atmosphere and ocean operated on a diurnal time scale. With a relatively shallow ML, the upper ocean structure

information). The results revealed an increase of approximately 16% (24%) of the latent (sensible) heat flux in the experiment fixed-0402, compared with the fully coupled simulation. This again indicates that the surface heat fluxes were insufficient for the development of the Taiwan low in the fully coupled simulation.

Because solar radiation is the primary energy contributor to the ocean, surface restratification, and thus the diurnal SST signal, is sensitive to the optical absorbance of upper waters. *Dickey and Simpson* [1983] showed that a relatively high absorption of solar heating in the surface layer would intensify the diurnal SST amplitude and increase the upper ocean heat content. From a seasonal perspective, enhanced optical absorbance in the surface layer would result in warmer SSTs, a shallower ML, and a more intense thermocline [*Kara et al.*, 2005a, 2005b]. Specifically, the diurnal SST amplitude is sensitive to the preferential absorbance of the red portion of

responded favorably to the solar heating, leading to a recurrent diurnal surface restratification and diurnal fluctuation in the upper thermocline. The SST experienced apparent diurnal oscillations. Because the amounts of surface heat losses and entrainment cooling from below were relatively small, the nocturnal SST drop was limited at this time. The nocturnal cooling of the upper water layer could be alleviated or even overwhelmed by a lateral heat transport at some locations. Consequently, an insolation-induced SST warming trend occurred during this stage. The upper ocean heat content increased prior to the frontal passage.

During the cold-air outbreak, the strong wind burst led to a significant cooling of the upper ocean, mainly caused by wind-driven mixing and turbulent heat loss from the surface. The SST diurnal cycle vanished because the high wind speeds generated sufficient vertical mixing to destroy any insolation-induced thermal stratification. The wind-driven vertical mixing entrained cooler sublayer water from below, eroded the upper seasonal thermocline, and deepened the ML. Cooling throughout the upper water column manifested a loss of upper ocean heat content, which was primarily determined by the amount of surface heat loss and entrained cool water. The SST dropped accordingly. The strong wind stirring left behind a deeper, cooler, and less stratified remnant layer. The thick remnant layer acted to decouple the sublayer cooler water from the surface boundary layer. Because less heat was trapped to form a diurnal warm layer, surface restratification was suppressed. The retreat of the Kuroshio in response to the strong wind burst was overestimated. This caused a feedback of degraded SSTs to the atmosphere, which may have preconditioned the stagnation of the Taiwan low in the model. The results of sensitivity experiments with fixed SSTs support the argument about the ocean preconditioning of the Taiwan low.

Under calm weather conditions, the ocean gains heat; it loses heat to the atmosphere when the system is disturbed by strong winds. Even though such weather events may be short lived, the resulting convective and wind-driven boundary layers can penetrate well into the stratified sublayer (the upper seasonal thermocline) below the ML; thus, strong weather may have a significant impact on a markedly longer time scale to shape climate variability. Surface restratification is one of the major contributors to the recovery of upper ocean heat content. Lateral heat supply and/or penetrated solar radiation can also contribute to the warming of upper waters. These heat fluxes can maintain a weak ambient stratification and can also be a heat source for local surface heat losses.

The vertical resolution in our model was insufficient to fully resolve the near-surface physics involved with the surface diurnal cycle. The near-surface physics is perhaps the most imperative portion to be improved in the coupled modeling system. A longer integration is necessary to systematically evaluate the near-surface physics under a variety of weather situations in a particular season and to assess the biases that can accumulate into the seasonal mean. We leave this for future research to investigate.

Acknowledgments

All data for this paper are properly cited and referred to in the reference list. The authors thank the Editor and two anonymous reviewers for their valuable comments and suggestions that significantly improved this paper. The first author was funded by the Postdoctoral Program of the National Central University, Taiwan. This research was partially supported by the National Science Council in Taiwan under grants NSC 100-2119-M-008-041-MY5 and MOST 101-2517-S-008-002-MY3b.

References

- Andres, M., J.-H. Park, M. Wimbush, X.-H. Zhu, K.-I. Chang, and H. Ichikawa (2008a), Study of the Kuroshio/Ryukyu Current system based on satellite-altimeter and in situ measurements, *J. Oceanogr.*, 64(6), 937–950.
- Andres, M., M. Wimbush, J.-H. Park, K.-I. Chang, B.-H. Lim, D. R. Watts, H. Ichikawa, and W. J. Teague (2008b), Observations of Kuroshio flow variations in the East China Sea, *J. Geophys. Res.*, 113, C05013, doi:10.1029/2007JC004200.
- Bane, J. M., Jr., and K. Osgood (1989), Wintertime air-sea interaction processes across the Gulf Stream, *J. Geophys. Res.*, 94, 10,755–10,722, doi:10.1029/JC094iC08p10755.
- Bernie, D. J., S. J. Woolnough, J. M. Slingo, and E. Guilyardi (2005), Modeling of diurnal and intraseasonal variability of the ocean mixed layer, *J. Clim.*, 18, 1190–1202.
- Bettencourt, M. T. (2002), Distributed model coupling framework, in Proc. HPDC-11.
- Bleck, R. (2002), An oceanic general circulation model framed in hybrid isopycnic-Cartesian coordinates, *Ocean Model.*, 4, 55–88.
- Brainerd, K. E., and M. C. Gregg (1993a), Diurnal restratification and turbulence in the oceanic surface mixed layer: 1. Observation, *J. Geophys. Res.*, 98, 22,645–22,656, doi:10.1029/93JC02297.
- Brainerd, K. E., and M. C. Gregg (1993b), Diurnal restratification and turbulence in the oceanic surface mixed layer: 2. Modeling, *J. Geophys. Res.*, 98, 22,657–22,664, doi:10.1029/93JC02298.
- Browning, G. L., and H. O. Kreiss (1982), Initialization of the shallow water equations with open boundaries by the bounded derivative method, *Tellus*, 34, 334–351.
- Caniaux, G., and S. Planton (1998), A three-dimensional ocean mesoscale simulation using data from the SEMAPHORE experiment: Mixed layer heat budget, *J. Geophys. Res.*, 103, 25,081–25,099.
- Chang, C.-B., D. J. Perkey, and W.-D. Chen (1987), Observed dynamic structure of an intense oceanic cyclone, *Mon. Weather Rev.*, 115, 1127–1139.
- Chassignet, E. P., L. T. Smith Jr., G. R. Halliwell, and R. Bleck (2003), North Atlantic simulations with the hybrid coordinate ocean model (HYCOM): Impact of the vertical coordinate choice, reference density, and thermobaricity, *J. Phys. Oceanogr.*, 34, 2504–2526.
- Chen, G. T. J., and C. F. Lu (1997), On the climatological aspects of explosive cyclones over the western north Pacific and East Asia coastal areas, *Terr. Atmos. Oceanic Sci.*, 8, 427–442.

- Chen, S.-J., and L. Dell'osso (1987), A numerical case study of East Asian coastal cyclogenesis, *Mon. Weather Rev.*, 115, 477–487.
- Chou, M.-D., and M. J. Suarez (1994), An efficient thermal infrared radiation parameterization for use in general circulation models, *NASA Tech. Memo.*, 104606, 3, 85 pp.
- Cronin, M., N. A. Bond, J. T. Farrar, H. Ichikawa, S. R. Jayne, Y. Kawai, M. Konda, B. Qiu, L. Rainville, and H. Tomita (2013), Formation and erosion of the seasonal thermocline in the Kuroshio Extension Recirculation Gyre, *Deep Sea Res., Part II*, 85, 62–74.
- Dickey, T. D., and J. J. Simpson (1983), The influence of optical water type on the diurnal response of the upper ocean, *Tellus*, 35B, 142–154.
- Fang, Y., Y. Zhang, J. Tang, and X. Ren (2010), A regional air-sea coupled model and its application over East Asia in the summer of 2000, *Adv. Atmos. Sci.*, 27, 583–593.
- Grell, G. A., J. Dudhia, and D. R. Stauffer (1995), A description of the fifth generation Penn State/NCAR mesoscale mode (MM5), *Tech. Note NCAR/TN-398+STR*, 122 pp., Natl. Cent. for Atmos. Res., Boulder, Colo.
- Halliwell, G. R. (2004), Evaluation of vertical coordinate and vertical mixing algorithms in the HYbrid Coordinate Ocean Model (HYCOM), *Ocean Modell.*, 7, 285–322.
- Hanson, H. P., and B. Long (1985), Climatology of cyclogenesis over the East China Sea, *Mon. Weather Rev.*, 113, 697–707.
- Hong, S.-Y., J. Dudhia, and S.-H. Chen (2004), A revised approach to ice microphysical processes for the bulk parameterization of clouds and precipitation, *Mon. Weather Rev.*, 132, 103–120.
- Hong, S.-Y., Y. Noh, and J. Dudhia (2006), A new vertical diffusion package with an explicit treatment of entrainment processes, *Mon. Weather Rev.*, 134, 2318–2341.
- Hosegood, P., M. C. Gregg, and M. H. Alford (2008), Restratification of the surface mixed layer with submesoscale lateral density gradients: Diagnosing the importance of the horizontal dimension, *J. Phys. Oceanogr.*, 38, 2438–2460.
- Huffman, G. J., et al. (2007), The TRMM Multisatellite Precipitation Analysis (TMPA): Quasi-global, multiyear, combined-sensor precipitation estimates at fine scales, *J. Hydrometeorol.*, 8, 38–55, doi:10.1175/JHM560.1.
- Ichikawa, H., and R. C. Beardsley (1993), Temporal and spatial variability of volume transport of the Kuroshio in the East China Sea, *Deep Sea Res., Part I*, 40, 583–605.
- Iwasaki, S., A. Isobe, and S. Kako (2014), Atmosphere-ocean coupled process along coastal areas of the Yellow and East China Seas in winter, *J. Clim.*, 27, 155–167.
- Jerlov, N. G. (1976), *Marine Optics*, Elsevier, New York.
- Jin, B., G. Wang, Y. Liu, and R. Zhang (2010), Interaction between the East China Sea Kuroshio and the Ryukyu Current as revealed by the self-organizing map, *J. Geophys. Res.*, 115, C12047, doi:10.1029/2010JC006437.
- Johns, W. E., T. N. Lee, D. Zhang, and R. Zantopp (2001), The Kuroshio east of Taiwan: Moored transport observations from the WOCE PCM-1 array, *J. Phys. Oceanogr.*, 31, 1031–1053.
- Jones, P. W. (2001), A user's guide for SCRIP: A spherical coordinate remapping and interpolation package, Version 1.4. 27pp. [Available at <http://climate.lanl.gov/Software/SCRIP/SCRIPUsers.pdf>.]
- Jullien, S., P. Marchesiello, C. E. Menkes, J. Lefevre, N. C. Jourdain, G. Samson, and M. Lengaigne (2014), Ocean feedback to tropical cyclones: Climatology and processes, *Clim. Dyn.*, 43, 2831–2854, doi:10.1007/s00382-014-2096-6.
- Kain, J. S. (2004), The Kain-Fritsch convective parameterization: An update, *J. Appl. Meteorol.*, 43, 170–181.
- Kako, S., and M. Kubota (2007), Variability of mixed layer depth in Kuroshio/Oyashio Extension region: 2005–2006, *Geophys. Res. Lett.*, 34, L11612, doi:10.1029/2007GL030362.
- Kara, A. B., A. J. Wallcraft, and H. E. Hurlbut (2005a), A new solar radiation penetration scheme for use in ocean mixed layer studies: An application to the Black Sea using a fine-resolution Hybrid Coordinate Ocean Model (HYCOM), *J. Phys. Oceanogr.*, 35, 13–32, doi:10.1175/JPO2677.1.
- Kara, A. B., A. J. Wallcraft, and H. E. Hurlbut (2005b), Sea surface temperature sensitivity to water turbidity from simulations of the turbid Black Sea using HYCOM, *J. Phys. Oceanogr.*, 35, 33–54.
- Kato, K., and Y.-M. Kodama (1992), Formation of the quasi-stationary Baiu front to the south of the Japan islands in early May of 1979, *J. Meteorol. Soc. Jpn.*, 70, 631–647.
- Kawai, Y., and A. Wada (2007), Diurnal sea surface temperature variation and its impact on the atmosphere and ocean: A review, *J. Oceanogr.*, 63, 721–744, doi:10.1007/s10872-007-0063-0.
- Kim, E.-J., and S.-Y. Hong (2010), Impact of air-sea interaction on East Asian summer monsoon climate in WRF, *J. Geophys. Res.*, 115, D19118, doi:10.1029/2009JD013253.
- Kondo, J. (1976), Heat balance of the East China Sea during the air mass transformation experiment, *J. Meteorol. Soc. Jpn.*, 54, 382–398.
- Large, W. G., J. C. McWilliams, and S. C. Doney (1994), Oceanic vertical mixing: A review and a model with a nonlocal boundary layer parameterization, *Rev. Geophys.*, 32, 363–403, doi:10.1029/94RG01872.
- Lee, T. N., W. E. Johns, C.-T. Liu, D. Zhang, R. Zantop, and Y. Yang (2001), Mean transport and seasonal cycle of the Kuroshio east Taiwan with comparison to the Florida Current, *J. Geophys. Res.*, 106(C10), 22,143–22,158, doi:10.1029/2000JC000535.
- Li, Y., H. Xue, and J. M. Bane (2002), Air-sea interactions during the passage of a winter storm over the Gulf Stream: A three dimensional coupled atmosphere-ocean model study, *J. Geophys. Res.*, 107, 3200, doi:10.1029/2001JC001161.
- Liu, Z., and J. Gan (2012), Variability of the Kuroshio in the East China Sea derived from satellite altimetry data, *Deep Sea Res., Part I*, 59, 25–36.
- Minobe, S., A. Kuwano-Yoshida, N. Komori, S.-P. Xie, and R. J. Small (2008), Influence of the Gulf Stream on the troposphere, *Nature*, 452, 206–209.
- Misra, V., L. Marx, M. Brunke, and X. Zeng (2008), The equatorial Pacific cold tongue bias in a coupled climate model, *J. Clim.*, 21, 5852–5869.
- Mlawer, E. J., S. J. Taubman, P. D. Brown, M. J. Iacono, and S. A. Clough (1997), Radiative transfer for inhomogeneous atmosphere: RRTM, a validated correlated-k model for the longwave, *J. Geophys. Res.*, 102(D14), 16,663–16,682, doi:10.1029/97JD00237.
- Nakada, Y. (1991), Appearance of stratiform clouds over south China and their relation to synoptic fields during the winter monsoon season, *Geogr. Rev. Jpn.*, 64A, 327–346.
- Ninomiya, K. (1977), Heat energy budget of the polar air-mass transformed over the Kuroshio region under the situation of strong subsidence, *J. Meteorol. Soc. Jpn.*, 55, 431–441.
- Paulson, C. A., and J. J. Simpson (1977), Irradiance measurements in the upper ocean, *J. Phys. Oceanogr.*, 7, 953–956.
- Persson, P. O. G., J. E. Hare, C. W. Fairall, and W. D. Otto (2005), Air-sea interaction processes in warm and cold sectors of extratropical cyclonic storms observed during FASTEX, *Q. J. R. Meteorol. Soc.*, 131, 877–912, doi:10.1256/qj.03.181.
- Price, J. F., R. A. Weller, and R. Pinkel (1986), Diurnal cycling, observations and models of the upper ocean response to diurnal heating, cooling and wind mixing, *J. Geophys. Res.*, 91, 8411–8427, doi:10.1029/JC091iC07p08411.
- Ren, X., and Y. Qian (2005), A coupled regional air-sea model, its performance and climate drift in simulation of the East Asian summer monsoon in 1998, *Int. J. Climatol.*, 25, 679–692.

- Saha, S., et al. (2010), The NCEP climate forecast system reanalysis, *Bull. Am. Meteorol. Soc.*, **91**, 1015–1057.
- Sasaki, Y. N., S. Minobe, T. Asai, and M. Inatsu (2012), Influence of the Kuroshio in the East China Sea on the early summer (Baiu) rain, *J. Clim.*, **27**, 6627–6645.
- Seo, H., and S.-P. Xie (2013), Impact of ocean warm layer thickness on the intensity of hurricane Katrina in a regional coupled model, *Meteorol. Atmos. Phys.*, **122**, 19–32, doi:10.1007/s00703-013-0275-3.
- Shinoda, T. (2005), Impact of diurnal cycle of solar radiation on intraseasonal SST variability in the western equatorial Pacific, *J. Clim.*, **18**, 2628–2636.
- Shiota, M., R. Kawamura, H. Hatsushika, and S. Iizuka (2011), Influence of the East Asian winter monsoon variability on the surface cyclogenesis over the East China Sea in late winter, *Sci. Online Lett. Atmos.*, **7**, 129–132.
- Skamarock, W. C., et al. (2008), A description of the Advanced Research WRF version 3, *NCAR Tech. Note TN-475STR*, 125 pp.
- Small, R. J., S. P. de Szoeke, S. P. Xie, L. O'Neill, H. Seo, Q. Song, P. Cornillon, M. Spall, and S. Minobe (2008), Air-sea interaction over ocean fronts and eddies, *Dyn. Atmos. Oceans*, **45**, 274–319.
- Stauffer, D. R., and N. L. Seaman (1990), Use of four-dimensional data assimilation in a limited area mesoscale model. Part I: Experiments with synoptic-scale data, *Mon. Weather Rev.*, **118**, 1250–1277.
- Tewari, M., F. Chen, W. Wang, J. Dudhia, M. A. LeMone, K. Mitchell, M. Ek, G. Gayno, J. Wegiel, and R. H. Cuenca (2004), Implementation and verification of the unified NOAH land surface model in the WRF model, paper presented at 20th conference on weather analysis and forecasting/16th conference on numerical weather prediction, pp. 11–15, Am. Meteorol. Soc., Seattle, Wash.
- Thiébaux, J., E. Rogers, W. Wang, and B. Katz (2003), A new high resolution blended real-time global sea surface temperature analysis, *Bull. Am. Meteorol. Soc.*, **84**, 645–656, doi:10.1175/BAMS-84-5-645.
- Tozuka, T., and M. F. Cronin (2014), Role of mixed layer depth in surface frontogenesis: The Agulhas return current front, *Geophys. Res. Lett.*, **41**, 2447–2453, doi:10.1002/2014GL059624.
- Wallcraft, A. J., E. J. Metzger, and S. N. Carroll (2009), HYCOM Design Description for the HYbrid Coordinate Ocean Model (HYCOM) Version 2.2, Tech. rep., Naval Res. Lab., Stennis Space Center, Miss.
- Woolnough, S. J., F. Vitart, and M. A. Balmaseda (2007), The role of the ocean in the Madden-Julian Oscillation: Implications for MJO prediction, *Q. J. R. Meteorol. Soc.*, **133**, 117–128.
- Xie, S.-P., J. Hafner, Y. Tanimoto, W. T. Liu, H. Tokinaga, and H. Xu (2002), Bathymetric effect on the winter sea surface temperature and climate of the Yellow and East China Seas, *Geophys. Res. Lett.*, **29**(24), 2228, doi:10.1029/2002GL015884.
- Xu, H., M. Xu, S.-P. Xie, and Y. Wang (2011), Deep atmospheric response to the spring Kuroshio over the East China Sea, *J. Clim.*, **24**, 4959–4972.
- Xue, H., J. M. Bane Jr., and L. M. Goodman (1995), Modification of the Gulf Stream through strong air-sea interaction in winter: Observations and numerical simulation, *J. Phys. Oceanogr.*, **25**, 533–557.
- Yu, C. C. (1980), Some climatological aspects of Taiwan low, *Paper Meteorol. Res.*, **3**, 78–90.
- Yu, L., and M. J. McPhaden (2011), Ocean preconditioning of Cyclone Nargis in the Bay of Bengal: Interaction between Rossby waves, surface fresh waters, and sea surface temperatures, *J. Phys. Oceanogr.*, **41**, 1741–1755, doi:10.1175/2011JPO4437.1.
- Yu, L., and R. A. Weller (2007), Objectively analyzed air-sea heat fluxes (OAFlux) for the global oceans, *Bull. Am. Meteorol. Soc.*, **88**, 527–539.
- Yu, L., X. Jin, and R. A. Weller (2008), Multidecade global flux datasets from the objectively analyzed air-sea fluxes (OAFlux) project: Latent and sensible heat fluxes, ocean evaporation, and related surface meteorological variables, *OAFlux Project Tech. Rep.*, Woods Hole Oceanographic Institution, Woods Hole, Mass.
- Zou, L., and T. Zhou (2011), Sensitivity of a regional ocean atmosphere coupled model to convection parameterization over western North Pacific, *J. Geophys. Res.*, **116**, D18106, doi:10.1029/2011JD015844.